

Improving Damped Random Walk parameters for SDSS Stripe 82 Quasars with Pan-STARRS1

KRZYSZTOF L. SUBERLAK,¹ ŽELJKO IVEZIĆ,¹ AND CHELSEA MACLEOD²

¹*Department of Astronomy, University of Washington, Box 351580, Seattle, WA 98195, USA*

²*Harvard Smithsonian Center for Astrophysics, 60 Garden Street, Cambridge, MA 02138, USA*

(Received November 8, 2019)

Submitted to ApJ

ABSTRACT

We use the Panoramic Survey Telescope and Rapid Response System 1 Survey (Pan-STARRS1, PS1) data to extend the Sloan Digital Sky Survey (SDSS) Stripe 82 quasar light curves. Combining PS1 and SDSS light curves provides 15 years baseline for 9248 quasars - 5 years longer than prior studies that used only SDSS. We fit the light curves with Damped Random Walk (DRW) model, and correlate the DRW model parameters - asymptotic variability amplitude SF_{∞} , and characteristic timescale τ , with quasar physical properties - black hole mass, bolometric luminosity, and redshift. Using simulated light curves, we find that longer baseline allows us to better constrain DRW parameters. After adding PS1 data, the variability amplitude is a stronger function of the black hole mass, and has a weaker dependence on quasar luminosity. In addition, the characteristic timescale τ dependence on quasar luminosity is marginally weaker. We also make predictions for the fidelity of DRW model parameter retrieval when light curves will be further extended with Zwicky Transient Facility (ZTF) and the Rubin Observatory Legacy Survey of Space and Time (LSST) data. Finally, we show how updated DRW parameters lend an independent method of discovering Changing-Look Quasar Candidates (CLQSO). The candidates are outliers in terms of differences in magnitude and scatter between SDSS and PS1 segments. We identify 40 objects (35 newly reported) with tenfold increase in variability timescale between SDSS and SDSS-PS1 data, which is due to a large change in brightness (over 0.5 mag) - a characteristic for CLQSO.

1. INTRODUCTION

Quasars are variable at rest-frame optical wavelengths at the asymptotic root-mean-square (rms) level of about 0.2 mag. These distant galaxies harbor an actively accreting supermassive black hole - an active galactic nucleus. Although it is agreed upon that the majority of optical light originates from the thermal emission of the accretion disk, the detailed origin of variability has been debated for the past 50 years (see Sun et al. 2018 and references therein). Some favor a thermal origin of variability (Kelly et al. 2013), related to the propagation of inhomogeneities (‘hot spots’) in the disk (Dexter & Agol 2011; Cai et al. 2016), others suggested magnetically elevated disks (Dexter & Begelman 2019), or X-ray reprocessing (Kubota & Done 2018). Indeed, it may well be that the answer involves combination of these

- as Sánchez-Sáez et al. (2018) suggests, perhaps short-term variability (hours-days) is linked to the changes in X-ray flux, while long-term variability (months-years) is more intrinsic to the disk (Edelson et al. 2015; Lira et al. 2015). Nevertheless, quasar optical light curves have been successfully described using the Damped Random Walk (DRW) model (Kelly et al. 2009; MacLeod et al. 2010; Kozłowski et al. 2010; Zu et al. 2011; Kasliwal et al. 2015), and the DRW parameters have been linked to the physical quasar properties (MacLeod et al. 2010, hereafter M10).

Variability is also a classification tool, allowing to distinguish quasars from other variable sources that do not exhibit a stochastic variability pattern (MacLeod et al. 2011). This property is especially useful for selecting quasars in the intermediate redshift range, which overlaps the stellar locus in color-color diagrams (Sesar et al. 2007; Yang et al. 2017)). Variability has also been used to increase the completeness in measurements of Quasar Luminosity Function (see Ross et al. 2013; Palanque-

Delabrouille et al. 2013; AlSayyad 2016; McGreer et al. 2013, 2018).

Power spectral density (PSD) informs us about the distribution of variability across frequency range: from short timescales (high frequencies) to long timescales (low frequencies). Quasar, or more broadly speaking, AGN variability, exhibits a broken power law PSD, of the form $\log P(f) \propto \alpha_l \log(f)$, with α_l at low frequencies and α_h at high frequencies. For a pure DRW process, $\alpha_h = -2$ and $\alpha_l = 0$, so that:

$$P(f) = \frac{4\sigma^2\tau}{1 + (2\pi\tau f)^2} \quad (1)$$

(with $\sigma = \text{SF}_\infty/\sqrt{2}$, τ the characteristic timescale, f the frequency), where $P(f) \propto f^{-2}$ at high frequencies $f > (2\pi\tau)^{-1}$, and levels to a constant value at lower frequencies (Kelly et al. 2014).

There is a debate in the literature about the exact shape of the quasar PSD, and of any possible departures from the pure DRW model. Studies using quasar data from wide-field photometric surveys (OGLE, SDSS, PS1) benefit from relatively long baselines (several years), which constrain the low frequency part of the PSD. Overall, there is no evidence of a significant departure from DRW at these long timescales, i.e. $\alpha_l \approx 0$ (Zu et al. 2013; Simm et al. 2016; Kozłowski 2016; Caplar et al. 2017; Guo et al. 2017; Sun et al. 2018). However, these ground-based surveys suffer from a sparse sampling, which can be remedied by using a space-based telescope that can carry out near-continuous observations, like the Kepler mission (Borucki et al. 2010). Studies using Kepler data, that focused on a smaller number of well-sampled AGN with short baselines (<hundred days), found a range of power-law slopes at high frequencies - from -1 to -3.2, which includes the DRW $\alpha_h \approx -2$, but further study is needed (Mushotzky et al. 2011; Edelson et al. 2014; Aranzana et al. 2018; Smith et al. 2018). However, in this paper the timescales probed are larger than several days, and thus we can assume that DRW is the best working description of quasar variability for available optical light curves. Furthermore, in this work we directly compare the results of SDSS light curves extended with PS1 to M10 who used pure DRW description (see discussion therein on a possible departure from DRW). Therefore, to allow a better comparison of our results with M10, we use the DRW description of quasar PSD.

Due to its stochastic nature, for an unbiased parameter retrieval of DRW process the light curve is required to be several times longer than the characteristic timescale (Kozłowski et al. 2010; Kozłowski, Szymon 2017, hereafter K17). This means that DRW parameters

recovered for short light curves (compared to the recovered timescale) may be biased, which in turn affects the correlations with physical parameters (black hole mass, Eddington ratio, absolute luminosity).

For this reason, while some studies have restricted the probed redshift range, limiting the quasar sample to where one would expect only shorter timescales based on previous studies (Sun et al. 2018; Guo et al. 2017; Kelly et al. 2013; Simm et al. 2016), some have elected not to study timescales at all (Sun et al. 2018; Sánchez-Sáez et al. 2018), or use the timescales recovered from short light curves primarily for classification (Hernitschek et al. 2016).

By extending available quasar light curves, we are able to better recover DRW timescales. Since almost a decade ago, when M10 published their study based on SDSS Stripe 82 data, new datasets (PS1, PTF, CRTS) have become available. They can extend the quasar light curves by almost 50%. Indeed, Li et al. (2018) combined SDSS and Dark Energy Camera Legacy Survey (DECaLS) data, to provide a 15 year baseline, but by using the entire SDSS footprint suffered from poor sampling and had to use the ensemble structure function approach.

Unlike previous studies, in this work, by combining SDSS and PS1 data for the well-observed Stripe 82, we afford both an extended baseline (15 years), a large number (9000) of quasars, and a good cadence ($N > 60$ epochs) to which we fit the DRW model. The layout of this paper is as follows: first we confirm in Section 2 that extending the quasar baseline is an important improvement in providing unbiased estimates of the DRW model parameters (K17); in Section 3 we describe the datasets employed, and their combination onto a common photometric system; in Section 4 we simulate the improvement in the recovery of DRW parameters with baseline extension and realistic cadence; finally in Section 5 we describe the main results analyzing correlations between physical parameters and variability, in Section 6 we discuss the physical meaning of relevant timescales, and in Section 7 we summarize the main conclusions. In this work we adopt a Λ CDM cosmology with $h_0 = 0.7$ and $\Omega_m = 0.3$.

2. METHODS

2.1. DRW as a Gaussian Process

Damped Random Walk (Ornstein-Uhlenbeck process, Rasmussen & Williams 2006) can be modeled as a member of a class of Gaussian Processes (GP). Each GP is described by a mean and a kernel - a covariance function that contains a measure of correlation between two points: x_n and x_m , separated by Δt_{nm} (autocorrela-

tion). For the DRW process, the covariance between two observations spaced by Δt_{nm} is:

$$\begin{aligned} k(\Delta t_{nm}) &= \sigma^2 \exp(-\Delta t_{nm}/\tau) \\ &= \sigma^2 \text{ACF}(\Delta t_{nm}) \end{aligned} \quad (2)$$

Here σ^2 is an amplitude of correlation decay as a function of Δt_{nm} , while τ is the characteristic timescale over which correlation drops by $1/e$. For a DRW, the correlation function $k(\Delta t_{nm})$ is also related to the autocorrelation function ACF.

Not explicitly used in this paper, but of direct relevance to the DRW modeling, is the structure function (SF). SF can be found from the data as the root-mean-square scatter of magnitude differences Δm calculated as a function of temporal separation Δt (we drop subscripts n, m for brevity). SF is directly related to a DRW kernel $k(\Delta t)$:

$$\text{SF}(\Delta t) = \text{SF}_\infty (1 - \exp(-|\Delta t|/\tau))^{1/2} \quad (3)$$

For quasars SF follows approximately a power law: $\text{SF} \propto \Delta t^\beta$, and for large time separation Δt , as epochs in the light curve cease to be correlated, it levels out to a constant value SF_∞ - the asymptotic SF. Note that σ in Eq. 2 is related to the asymptotic SF as $\text{SF}_\infty = \sqrt{2}\sigma$ (also see MacLeod et al. (2012); Bauer et al. (2009); Graham et al. (2015) for an overview).

2.2. Fitting

We evaluate the likelihood of the DRW model with a particular set of τ, σ given the data with celerite - a fast GP solver (Foreman-Mackey et al. 2017). The underlying matrix algebra is similar to that used by Rybicki & Press (1992), Kozłowski et al. (2010), and M10. Also, as in previous work, we use a prior on DRW parameters that is uniform in log space: $1/(\sigma\tau)$. The main difference in our approach is that rather than adopting the Maximum A-Posteriori (MAP) as the ‘best-fit’ value for the DRW parameters (as in Kozłowski et al. 2010, K17, Kozłowski 2016, M10, MacLeod et al. 2011), we find the expectation value of the marginalized posterior. This is advantageous because of a non-Gaussian shape of the posterior - otherwise, if the posterior was a 2D normal distribution, the expectation value would coincide with the maximum of the posterior (MAP solution).

2.3. The impact of light curve baseline

K17 reports that one cannot trust any results of DRW fitting unless the light curve length is at least ten times longer than the characteristic timescale. In this section we revisit the relationship between recovered and input

timescales as a function of light curve baseline by following K17 setup. We confirm that the bias in retrieved DRW timescale depends on how many times the light curve is longer than the timescale. However, we find that the baseline does not have to be as many as ten times longer to provide meaningful, rather than unconstrained, results. Assuming fixed baseline of $\Delta T = 8$ years, we simulate 10 000 light curves, exploring 100 values of input timescales, but identical $\text{SF}_\infty = 0.2$ mag, with either SDSS ($N = 60$), or OGLE-like ($N = 445$) cadence. Defining ρ as the ratio of input timescale to baseline, we probe a range of ρ between 0.01 and 15, uniform in a logarithmic grid.

For each light curve we simulate the underlying DRW signal $s(t)$ by iterating over the array of time steps t . At each step, we draw a point from a Gaussian distribution, for which the mean and standard deviation are re-calculated at each timestep (see eqs. A4 and A5 in Kelly et al. 2009, Sec. 2.2 in M10, and K17). Initially, at t_0 the signal is equal to the mean magnitude, $s_0 = \langle m \rangle$. After a timestep $\Delta t_i = t_{i+1} - t_i$, the signal s_{i+1} is drawn from a normal distribution $\mathcal{N}(\text{loc}, \text{stdev})$, with :

$$\text{loc} = s_i e^{-r} + \langle m \rangle (1 - e^{-r}) \quad (4)$$

and

$$\text{stdev}^2 = 0.5 \text{SF}_\infty^2 (1 - e^{-2r}) \quad (5)$$

where $r = \Delta t_i / \tau$, and τ is the damping timescale.

Like K17, we add to the true underlying signal with zero mean $s(t)$, a mean magnitude ($\text{r}_{\text{SDSS}} = 17$ mag and $\text{I}_{\text{OGLE}} = 18$ mag), and calculate magnitude-dependent estimate of photometric uncertainty:

$$\sigma_{\text{SDSS}}^2 = 0.013^2 + \exp[2(\text{r}_{\text{SDSS}} - 23.36)] \quad (6)$$

$$\sigma_{\text{OGLE}}^2 = 0.004^2 + \exp[1.63(\text{I}_{\text{OGLE}} - 22.55)] \quad (7)$$

To simulate observational conditions we add a Gaussian noise $n(t) = \mathcal{N}(0, \sigma(t))$:

$$y(t) = s(t) + n(t) \quad (8)$$

The resulting distribution of fitted timescales as a function of input timescales, scaled by the 8 year baseline: ρ_{out} vs ρ_{in} , is shown in Fig. 1. We confirm the findings of K17: for short light curves, the best-fit τ becomes $\sim 1/5$ of light curve length (where $\log_{10}(\rho_{\text{out}}) \approx -0.7$, the ‘unconstrained’ region, lower-left of each panel). However, as long as the light curve is several times longer than the timescale ($1/\rho \gtrsim 3$, i.e. $\log_{10}(\rho) \lesssim 0.5$), we can recover the timescale without substantial bias (the dashed line approaches the solid diagonal line on both

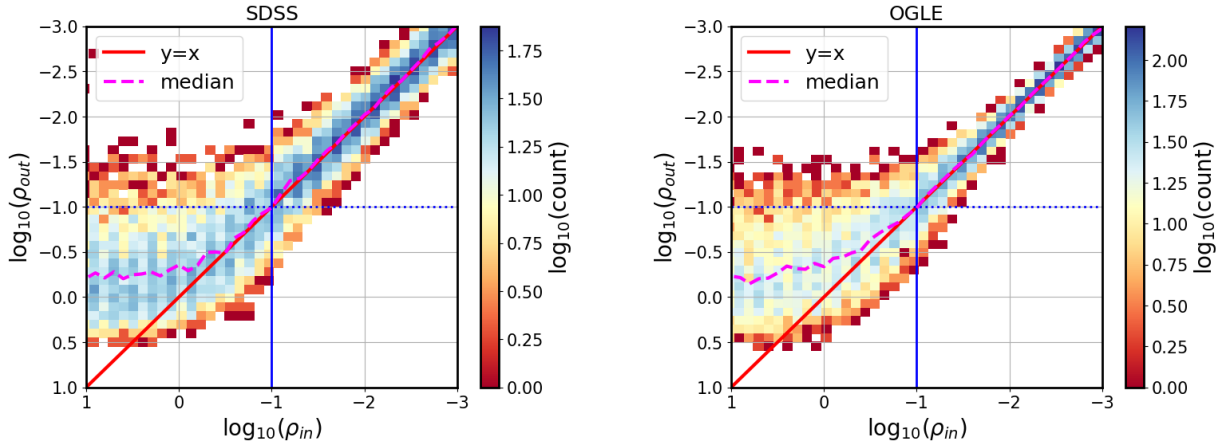


Figure 1. Recovery of the input DRW timescale, with baseline fixed to $\Delta T = 8$ years. We explore 100 logarithmically-spaced values of $\rho \equiv \tau/\Delta T$, simulating 100 realizations of DRW process at each ρ . The impact of photometric uncertainties and cadence is small in this case: the left panel (SDSS, $N=60$ epochs) does not significantly differ from the right panel (OGLE, $N=445$ epochs). The dotted horizontal and solid vertical lines mark $\rho = 0.1$, i.e. the baseline being ten times longer than the timescale. The solid diagonal line corresponds to a perfect recovery of DRW parameters (where $\rho_{in} = \rho_{out}$). For any quasar, extending its light curve moves it towards the upper-right (well-constrained) portion of the diagram, since for a fixed τ_{in} , increasing ΔT decreases ρ . For baselines shorter than τ , best-fit τ is underestimated and becomes biased to $\Delta T/2$.

panels). Therefore, by extending the baseline we can move from the biased region (bottom left) to the unbiased regime (top right). This is the basis for this study, in which we extend the baselines of quasar light curves from SDSS-only (10 years) to combined SDSS-PS1 (15 years).

3. DATA

We focus on the data pertaining to a 290 deg^2 region of the southern sky known as Stripe 82 (S82), repeatedly observed by the Sloan Digital Sky Survey (SDSS) between 1998 and 2008. Originally aimed at supernova discovery, objects in this area were re-observed on average 60 times (see MacLeod et al. 2012, Sec. 2.2 for overview, and Annis et al. 2014 for details). Availability of well-calibrated (Ivezić et al. 2007), long-baseline light curves spurred variability research (Sesar et al. 2007). The DR9 catalog (Schneider et al. 2008) contains 9258 spectroscopically confirmed quasars within S82. Within $0.5''$ we find matching data for 9248 quasars from Pan-STARRS1 (PS1) DR2 (Chambers et al. 2016; Flewelling et al. 2016; Flewelling 2018), 7737 from Catalina Real-Time Transient Survey (CRTS, Drake et al. 2009), 6455 from Palomar Transient Factory (PTF, Rau et al. 2009), and 8001 from Zwicky Transient Facility DR1 (ZTF, Bellm et al. 2019; Masci et al. 2019). Fig. 2 illustrates the improvement in baseline coverage when combining various surveys. The width of each rectangle corresponds to the duration of each survey (survey baseline), and the height to the area covered by each survey. The lower edge of each rectangle marks the 5σ depth in the

r-band (or equivalent). LSST stands out in that it will provide the best extension of SDSS baseline and depth.

Combining data from different photometric standards requires applying color transformation, or photometric offsets. We first seek to combine PS1 *gri*, PTF *gR*, and CRTS *V*, into a common SDSS *r*-band (best photometry). To this end we calculate color terms using the SDSS standard stars catalog (Ivezić et al. 2007). Focusing on a 100 000 randomly chosen stars, we find their CRTS, PS1, and PTF matches ¹.

The difference between the target (SDSS) and source (eg. PS1) photometry can be written as a function of the mean SDSS $g-i$ color:

$$m_{\text{PS1}} - m_{\text{SDSS}} = f(g-i) \quad (9)$$

Some authors (eg. Li et al. 2018) allow the transformation to be a higher-order polynomial, but as Fig. 3 shows, quasars occupy a relatively narrow region of $g-i$ color space, and we find that the linear fit is sufficient. The derived linear coefficients for photometric transformations between SDSS *r* and PS1 *gri*, PTF *gR*, CRTS *V*, as a function of SDSS $g-i$ color, are listed in Table 1. We illustrate the process showing in Fig. 4 the SDSS-PS1 standard stars data used to calculate the offsets. Note that the PS1 *r* (middle panel) is very close to the SDSS *r* - within 0.01 mag (1% level) across the $g-i$ color range. We focus on SDSS *r* - PS1 *r* offset as

¹ CRTS from B.Sesar, priv.comm., PS1 from MAST (<http://panstarrs.stsci.edu>), and PTF from IRSA PTF Object Catalog (<https://irsa.ipac.caltech.edu/>)

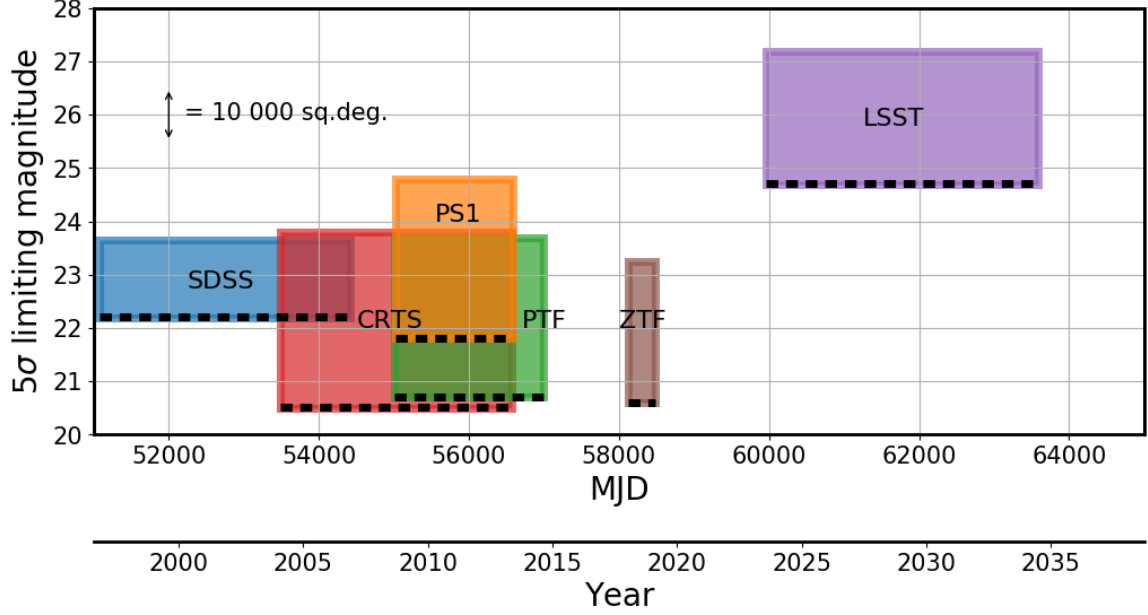


Figure 2. An illustration of survey baseline, sky area covered, and depth. The width of each rectangle corresponds to the extent of real or simulated light curves for Stripe 82 quasars for each survey. This includes SDSS DR7, CRTS DR2, PS1 DR2, PTF DR2, ZTF DR1, and for LSST the full 10-year survey. The lower edge of each rectangle (marked by a thick dashed line) corresponds to the 5σ limiting magnitude (SDSS r , PS1 r , PTF R , ZTF r , LSST r , CRTS V). The vertical extent of each rectangle corresponds to the total survey area (for SDSS, up to DR15). Note how PS1 and PTF extend the baseline of SDSS by approximately 50%, and how inclusion of LSST roughly triples the SDSS baseline. For reference, the area covered by LSST is 20000 sq.deg.

a function of magnitude in Fig. 5 - the near-equivalence of bandpass coverage is valid at 1% level up to $r < 20.5$.

In selecting the most beneficial datasets to complement SDSS r we also consider the associated photometric uncertainties (aka ‘errors’). As shown in Fig. 2, PTF and CRTS are shallower than SDSS or PS1. Therefore for faint objects, like quasars (for S82 sample the population median is SDSS $r \sim 20$ mag) PTF and CRTS have larger photometric uncertainties than SDSS or PS1. Indeed, as Fig. 6 shows, the distribution of median errors for PTF, CRTS, and ZTF quasar data is wider than the corresponding SDSS and PS1 data. As simulations show (Sec. 4), although PTF and CRTS data do extend the SDSS baseline, their error properties decreases their utility in complementing the SDSS dataset. After all, the SDSS baseline extension afforded with PTF and CRTS is comparable to that achieved with PS1 data alone (Fig. 2).

Furthermore, to mitigate problems that could arise when applying photometric transformations (such as spurious variability due to incorrect offsets, or color-dependent variability), we choose to combine SDSS r with only PS1 r , since as Figs. 4, 5 show, SDSS r and PS1 r are sufficiently similar (at 1% level up to 20.5 mag) that no photometric transformation is required.

Finally, we clean the combined SDSS r - PS1 r quasar light curves using standard procedures of σ -clipping in magnitude and error space, and error-weighted day-averaging, to mitigate the impact of bad photometry, and average out the intra-night variability (as in Charisi et al. 2016; Suberlak et al. 2017). Of 9248 SDSS-PS1 quasars, 8516 have the PS1 r data with 662 092 epochs. We remove points that have error departing from median SDSS(PS1) light curve segment by more than 7σ , and we visually inspect all photometry with magnitudes departing by more than 7σ from median magnitude. Of 585 flagged light curves, 253 required removal of individual epochs containing bad photometry. To avoid unphysically small errors, we add in quadrature 0.01 mag if combined nightly error is < 0.02 mag. In the final sample there are 580 321 epochs.

4. SIMULATIONS : LESSONS LEARNED

We simulate the theoretical improvement of the DRW parameter retrieval in extended light curves. We generate long and well-sampled ‘master’ light curves, all with input $\tau = 575$ days, $SF_{\infty} = 0.2$ mag (the median of S82 quasar distribution in M10), with 0 mean. We subsample at real observed epochs for SDSS and PS1, and at predicted cadences for ZTF and LSST (see Fig. 8). To each simulated light curve we add a magnitude offset

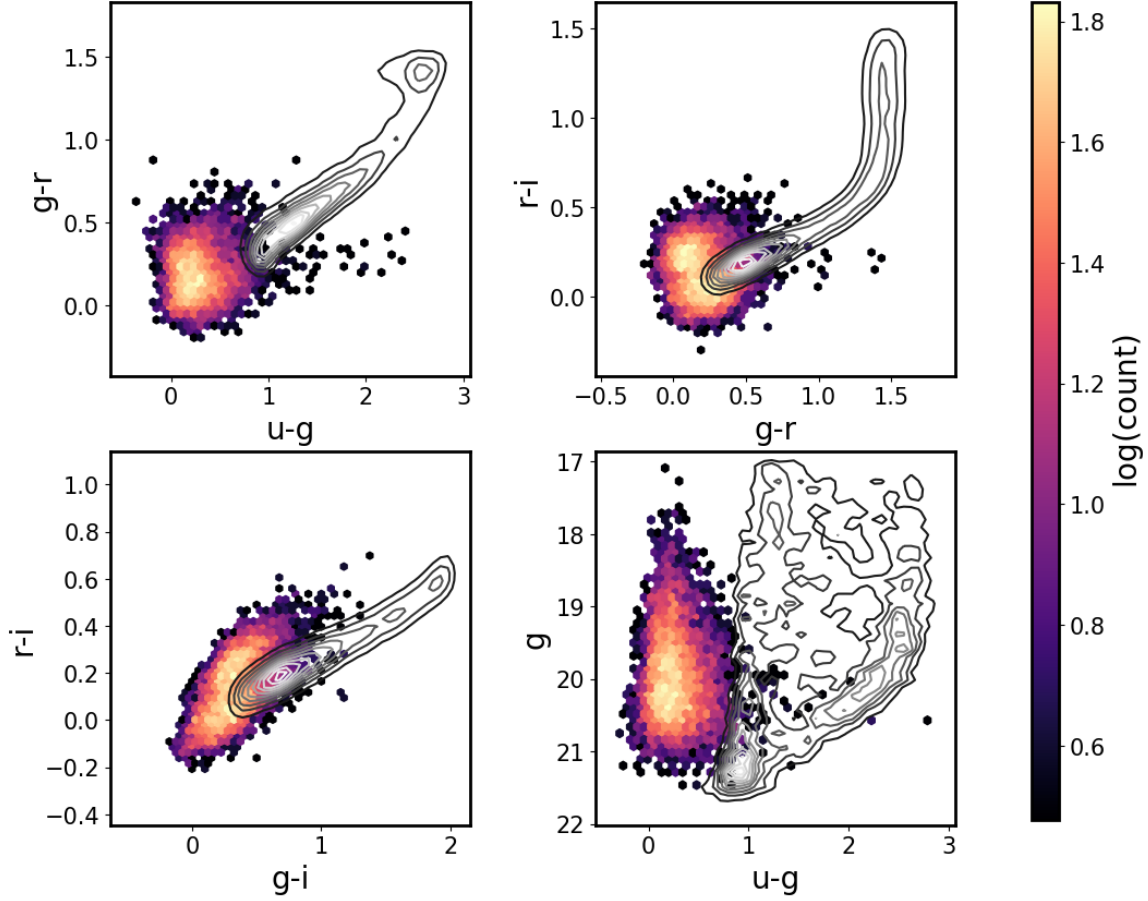


Figure 3. Regions of color-color (upper left, upper right, bottom left), and color-magnitude (bottom right) space occupied by SDSS S82 quasars (color) and stars (contours). We use quasar median photometry from [Schneider et al. \(2010\)](#), and standard stars catalog of [Ivezić et al. \(2007\)](#), showing a random subset of 10 000 stars. As seen in the bottom-left panel, quasars occupy a particular range of SDSS $g - i$ color. Therefore in fitting the linear color transformations we limit the color range to $-0.35 < (g - i) < 0.75$ (vertical dashed lines in Fig.4). Quasars also overlap other variable sources (eg. RR Lyrae), not shown here ([Sesar et al. 2007](#)).

corresponding to the mean of the combined SDSS-PS1 light curve. That way the magnitude distribution of simulated light curves is similar to that of the observed SDSS-PS1 data. For the LSST 10-year segment (finishing in 2031) we assumed 50 randomly distributed epochs per year, with the following error model:

$$\begin{aligned} \sigma_{LSST}(m)^2 &= \sigma_{sys}^2 + \sigma_{rand}^2 (\text{mag})^2 \\ \sigma_{rand}^2 &= (0.04 - \gamma)x + \gamma x^2 \\ x &= 10^{0.4(m-m_5)} \end{aligned} \quad (10)$$

with $\sigma_{sys} = 0.005$, $\gamma = 0.039$, $m_5 = 24.7$ (see [Ivezić et al. 2019](#), Sec. 3.2). For the ZTF 1-year segment (Spring 2019 ZTF DR1 including the data from 2018) we assumed 120 observations (every three nights) in g_{ZTF} and r_{ZTF} , deriving the magnitude-dependent error model by plotting best mag rms as a function of best median magnitude for ZTF matches to S82 stan-

dard stars in Fig. 7. We find that the LSST error model (Eq. 10) with $\gamma = 0.05$, $\sigma_{sys} = 0.005$, and $m_5 = 20.8$ adequately describes the ZTF photometric uncertainty.

To mirror observational conditions we add to the true underlying DRW signal a Gaussian noise, with variance defined by photometric uncertainties for corresponding surveys. Fig. 8 illustrates the simulated ‘master’ light curve (black dots, 4 per day), subsampled at SDSS (red), PS1 (green), and LSST (blue) cadence. While PS1 provides a 50% improvement of the SDSS baseline, LSST will nearly triple it. Fig. 9 shows how the simulated distribution of DRW parameters σ , τ , changes as the SDSS quasar light curves are extended with PS1, ZTF, and LSST data. In the future (after more data has been assembled and re-calibrated), ZTF will help, but not as dramatically as LSST. Note that ZTF, due to larger errors (Fig.6), causes a widening of the recovered τ distribution. Using PS1 data with its excellent deep pho-

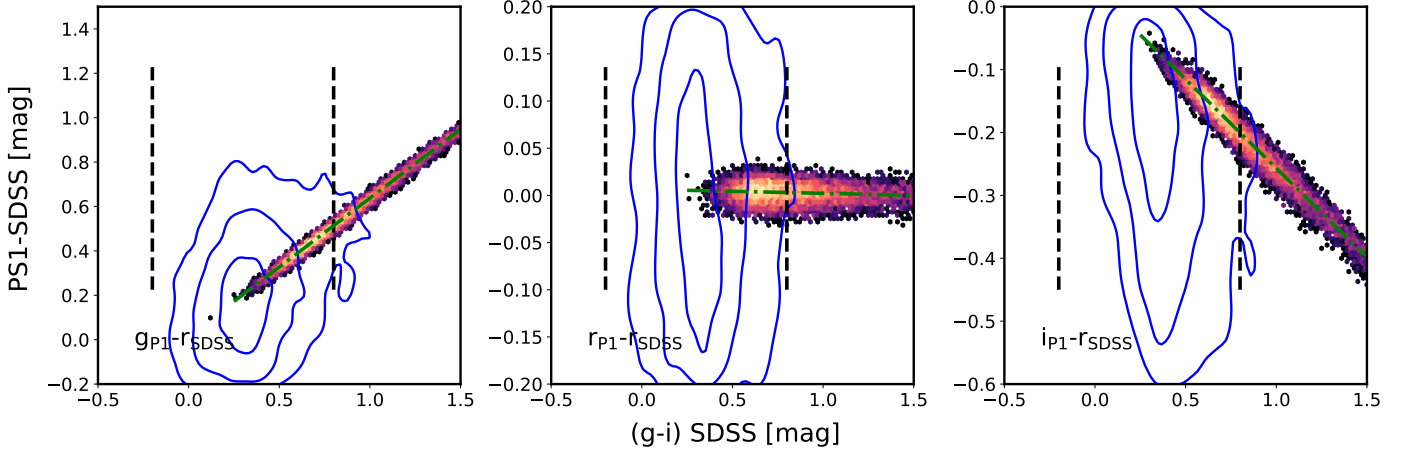


Figure 4. The SDSS-PS1 offsets, derived with the SDSS standard stars (Ivezić et al. 2007). From randomly chosen subset of 100 000 SDSS stars, 95 000 have PS1 DR2 data. To minimize scatter due to larger errors we select 40 000 stars with $r < 19$ mag. Vertical dashed lines mark the region in the SDSS color space occupied by quasars, indicated by the contours enclosing 90%, 70%, and 30% quasar data (also see Fig. 3). Stars with $-0.2 < g - i < 0.8$ were used to fit the stellar locus with a first order polynomial, marked by the dot-dashed line. The best-fit slopes: 0.619, -0.04, -0.283 for PS1 g , r , i , respectively, are listed as B_1 in Table 1.

Table 1. Color terms (photometric offsets) between CRTS, PTF, PS1 pass-bands and SDSS, using the SDSS mean $g-i$ color to spread the stellar locus. Thus the SDSS r synthetic magnitude, r_s , can be found as $r_s = x - B_0 - B_1(g-i)$. This linear trend is illustrated in Fig. 4, where we plot $(x - r_{\text{SDSS}})$ as a function of $(g-i)_{\text{SDSS}}$ for $x = g_{\text{P1}}, r_{\text{P1}}, i_{\text{P1}}$.

Band (x)	B_0	B_1
CRTS V	-0.0464	-0.0128
PTF g	-0.0294	0.6404
PTF R	0.0058	-0.1019
PS1 g	0.0174	0.6194
PS1 r	0.0065	-0.0044
PS1 i	0.0260	-0.2830

NOTE—To derive the color terms we used a subset of 100 000 stars randomly chosen from the SDSS standard stars catalog (Ivezić et al. 2007). To minimize scatter we selected bright stars with $r < 19$ mag.

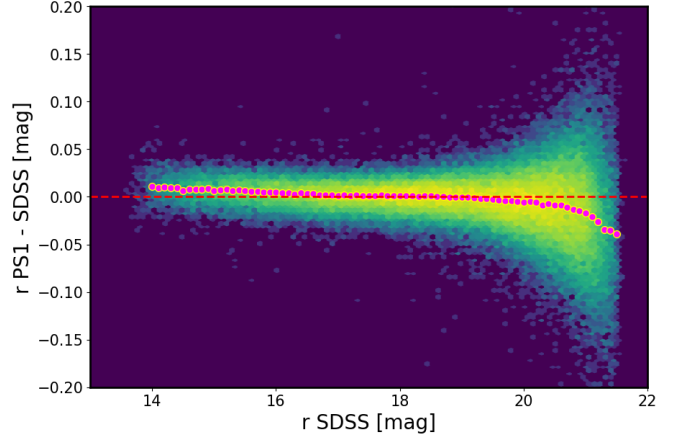


Figure 5. PS1 r vs SDSS r as a function of SDSS r for 100 000 randomly selected standard stars from Ivezić et al. (2007) catalog. Almost 95% of SDSS stars have PS1 DR2 photometry. The filled magenta circles represent the median offset - a slight slope at 1% (0.01 mag) level up to $r < 20.5$ mag.

tometry (as compared to ZTF or PTF) is the best improvement over existing SDSS results. For this reason we use only SDSS-PS1 portion of quasar light curves, as the best trade-off between adding more baseline vs introducing more uncertainty with noisy data.

5. RESULTS: VARIABILITY PARAMETERS FOR S82 QUASARS

We extend Stripe 82 quasar light curves by combining the SDSS r -band data with the PS1 r -band data,

without any photometric offsets. For each quasar we fit the SDSS and SDSS-PS1 segments with the DRW model. This yields two sets of DRW parameters per quasar: $(\tau_{\text{SDSS}}, \sigma_{\text{SDSS}})$, and $(\tau_{\text{SDSS-PS1}}, \sigma_{\text{SDSS-PS1}})$. Because variability is inherent to the quasar, for the remaining analysis we shift all fitted timescales to quasar rest frame, and implicitly assume that the DRW timescales are considered in rest frame: $\tau_{\text{RF}} = \tau_{\text{OBS}}/(1+z)$.

In this section we first correct fitted τ , σ for wavelength dependence. Then we show consistency with M10 results, and consider the trends between DRW param-

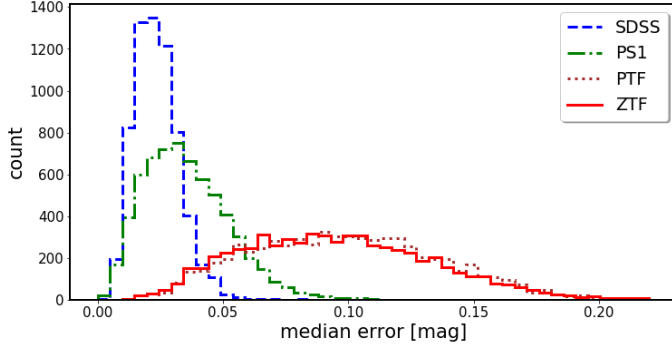


Figure 6. Distribution of median photometric uncertainties (‘errors’) in r-band real light curves. The PTF and ZTF segments have much larger errors than SDSS and PS1 due to shallower depth data. CRTS errors (not shown) are on average 50% larger than PTF.

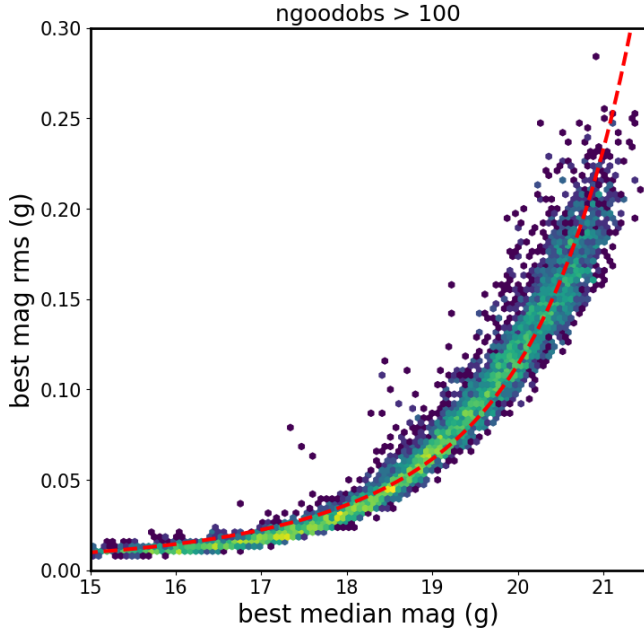


Figure 7. The best mag rms plotted as a function of magnitude for ZTF non-variable stars with over 100 observations. We overplot the adopted error model, with $\gamma = 0.05$, $\sigma_{sys} = 0.005$, and $m_5 = 20.8$ (see Eq. 10). Properties of ZTF photometric uncertainties are largely similar to the PTF uncertainties.

eters and physical quasar properties: black hole mass M_{BH} , absolute i-band magnitude M_i , or redshift z .

5.1. Comparison to M10

The DRW parameters recovered with *celerite* are broadly consistent with M10 - Fig. 10 shows the rest-frame τ , and SF_∞ distributions for our results for the SDSS segment (blue dashed contours), SDSS-PS1 combined light curves (green dot-dashed contours), and M10

SDSS for r-band only (red solid contours). When using exactly the same data as M10 (SDSS), our results agree. The offset of 0.05 dex between our and M10 results for SDSS, seen on the left panel of Fig. 11, can be attributed to data cleaning and software differences. The right panel of Fig. 11 shows the same distribution in terms of $K - \hat{\sigma}$ space, orthogonal to $\tau - \sigma$, where $\hat{\sigma} = \sigma\sqrt{2/\tau}$, and $K = \tau\sqrt{\sigma}2^{1/4}$.

5.2. Outliers: possible CLQSO candidates

Fig. 12 shows the change in recovered DRW parameters between SDSS and combined SDSS-PS1 light curves. The distribution of $f_\sigma \equiv \log_{10}(\sigma_{SDSS-PS1}/\sigma_{SDSS})$ and $f_\tau \equiv \log_{10}(\tau_{SDSS-PS1}/\tau_{SDSS})$ for real light curves (left), matches the predicted distribution for simulated light curves (right). Studies show that about 0.1% quasars will exhibit large variability (in excess of 0.5 mag rms - see Fig. 18 in MacLeod et al. 2012). Visual inspection of light curves in the upper-right region of the left panel of Fig. 12 (marked by the red rectangle) reveals large changes in brightness, similar to those seen in Changing-Look Quasars (MacLeod et al. 2019; Ruan et al. 2019; Sheng et al. 2019; Frederick et al. 2019; Trakhtenbrot et al. 2019; Shen et al. 2019; Stern et al. 2018; Ross et al. 2018; Lawrence 2018; Yang et al. 2018; Gezari et al. 2017; Stern et al. 2017; Sheng et al. 2017; Blanchard et al. 2017; Ruan et al. 2016; Runnoe et al. 2016; Guo et al. 2016; LaMassa et al. 2015; Schawinski et al. 2015; Elitzur et al. 2014). The light curves and properties of 38 CLQSO candidates for which $f_\tau > 1$, $f_\sigma > 0.4$, and $\langle r \rangle < 20.5$ are discussed in Appendix B.

Such large differences in timescales and amplitude of variability can also be inferred directly from the light curves. Consider the difference in magnitude and scatter between the SDSS portion of the light curve (spanning approximately 10 years between 1998 and 2008), and the PS1 portion (spanning ~ 5 years between, 2009-2014 - see Fig. 2). We measure the median magnitudes offset as $\Delta(\text{median}) = \text{median}(SDSS) - \text{median}(PS1)$, and the scatter difference as $\Delta(\sigma_G) = \sigma_G(SDSS) - \sigma_G(PS1)$. The resulting distributions of $\Delta(\text{median})$ and $\Delta(\sigma_G)$ for S82 quasars are shown in Fig. 14. Indeed, when plotting $\Delta(\text{median})$ as a function of f_τ and f_σ there is a gradient indicating that the CLQSO candidates - outliers in (f_τ, f_σ) space, are also outliers in $\Delta(\text{median})$ - $\Delta(\sigma_G)$ space. Thus the by-product of extending light curves to recalculate the DRW parameters with increased fidelity is an independent method to discover the CLQSO.

5.3. Rest-frame Wavelength Correction

Objects at cosmological distances are embedded in Hubble flow due to the expansion of the Universe (Riess

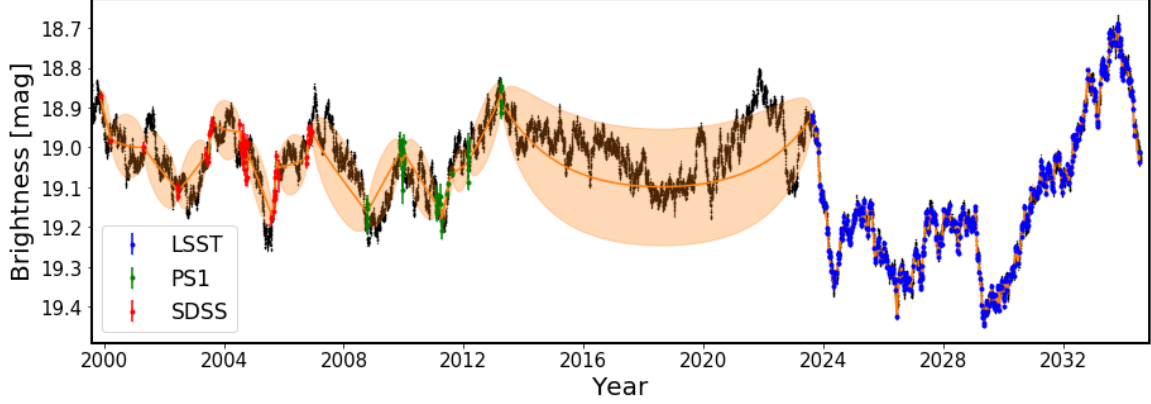


Figure 8. Simulated well-sampled underlying DRW process - one of ‘master’ light curves ($\tau = 575\text{d}$, $\text{SF}_\infty = 0.2\text{ mag}$, 4 points per day) shown with small black dots. To simulate observations, the cadence is degraded (subsampled) to match the ground-based cadence corresponding to real quasar data from SDSS (red), PS1 (green) segments, and simulated LSST (blue) epochs (here we use SDSS-PS1 epochs for quasar dbID=3537034). The orange ‘error snake’ is an envelope marking the standard deviation of the fit to the data using a Gaussian process with DRW kernel (Sec. 4).

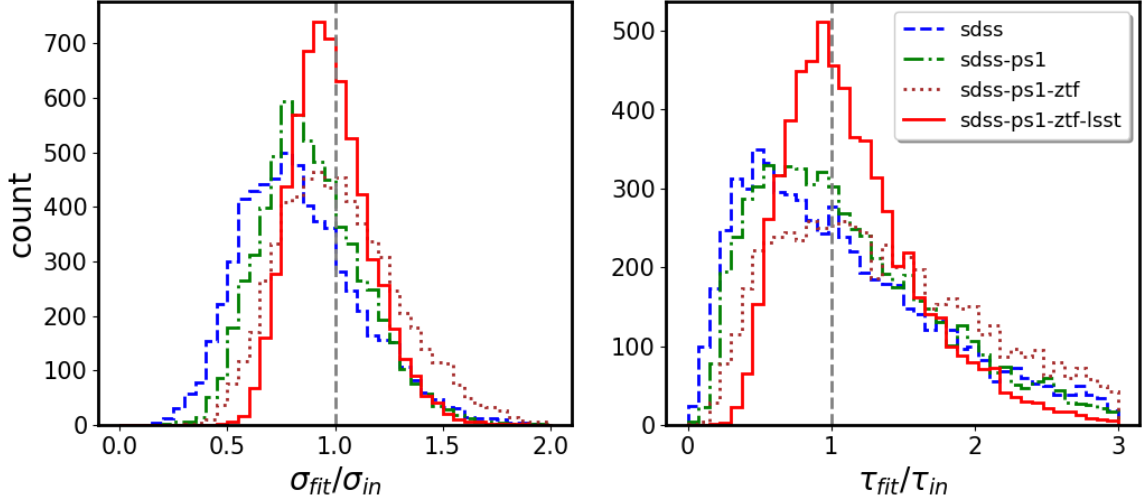


Figure 9. The ratio of DRW parameters fitted with *celerite*: τ and σ , to the input $\tau_{in} = 575\text{d}$, $\sigma_{in} = 0.2/\sqrt{2} \sim 0.14$ ($\text{SF}_\infty = 0.2\text{ mag}$). We simulated 9258 ‘master’ light curves, and subsampled at real SDSS r-band or PS1 r-band cadence and photometric uncertainties, and simulated ZTF and LSST cadence. To simulate observing conditions, the underlying DRW signal was convolved with a Gaussian noise corresponding to epochal errors. For each light curve we start with SDSS segment only, and as we add more segments (PS1, ZTF, LSST), we refit for DRW model parameters with *celerite*. Thus each distribution corresponds to a different segment of simulated combined SDSS-PS1-ZTF-LSST light curves. Extending the baseline shifts the distribution of recovered DRW parameters towards unbiased regime - vertical dashed line marks input matching the output. This corresponds to the upper-right (well-constrained) portion of Fig. 1.

et al. 2019). Therefore light observed from a distant quasar would have been emitted at shorter wavelength in quasar’s rest-frame: $\lambda_{RF} = \lambda_{obs}/(1+z)$, where z is the cosmological redshift. Quasars at different redshifts probe different regions of rest-frame spectra (see Fig.7 in Shen et al. 2019). Thus before correlating the DRW parameters with quasar properties we correct σ, τ for the λ_{RF} dependence, studied by M10 with SDSS *ugriz* light curves. We plot in Fig. 15 the DRW parameters:

SF_∞ and τ , as a function of λ_{RF} . A solid line marks the M10 best-fit power law trend:

$$f \propto \left(\frac{\lambda_{RF}}{4000\text{\AA}} \right)^B \quad (11)$$

with $B = -0.479$ and 0.17 for SF_∞ and τ , respectively.

5.4. Trends with Black Hole Mass, Absolute Luminosity

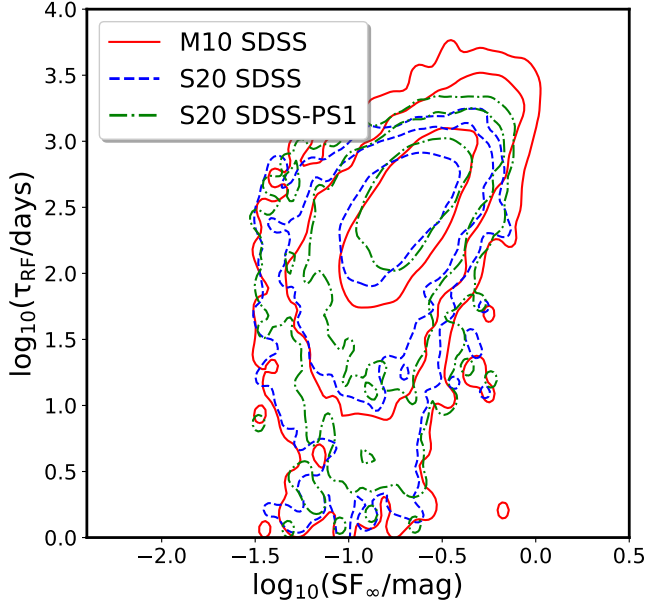


Figure 10. Comparison of distributions of the rest-frame variability timescale τ_{RF} against the asymptotic variability amplitude SF_{∞} , for M10 SDSS r -band (solid red) and *celerite* fits using SDSS (dashed blue) or SDSS-PS1 (dot-dashed green) segments of combined S82 quasar light curves. **Contours show the 1,2,3- σ levels (enclosing 68.3%, 95%, 99.7% of the data).** The timescales and SF_{∞} from M10 and this work overlap, as we recover the same underlying distributions.

In the era of large synoptic surveys such as ZTF or LSST, the large increase in the number of discovered quasars means that due to limited observational resources we will afford a spectroscopic follow-up for only a few percent of AGN with optical time-series (Ivezić et al. 2019). Therefore, a relationship between quasar variability parameters (τ, σ), and physical properties M_{BH} , M_i could provide an estimate of the latter for millions of quasars. We inspect correlations between τ, σ and M_{BH} , M_i , using Shen et al. (2011) catalog, based on single-epoch SDSS spectra. M_i is K-corrected to $z = 2$, corresponding to the peak of quasar activity (Richards et al. 2006). For details, see Appendix A.

On Fig. 16 we examine the distribution of M_{BH} , M_i , as a function of z for S82 quasars. The upward gradient in the top two panels reflects the selection effect that higher redshift quasars have to be brighter to be included in the magnitude-limited sample (luminosity-redshift degeneracy: see Sec.5, Fig.12 in M10, and Dong et al. 2018). Higher redshift quasars are also more active and have higher black hole masses due to cosmological downsizing (see Babić et al. 2007; Labita et al. 2009; McLure & Dunlop 2004). The distribution in the lower-

left panel of Fig. 16 is peaked at $z = 2$ which corresponds to the peak of quasar activity.

Fig. 17 shows the DRW parameters for S82 quasars: τ and SF_{∞} , plotted as a function of quasar physical properties M_{BH} , M_i , and z . Upper-left and lower-left panels in Fig. 17 contain a gradient of SF_{∞} with M_i, z - brighter quasars have lower variability amplitude, largely independent of black hole mass.

We investigate these relations in more detail by fitting f (τ or SF_{∞}) as a power-law function of M_{BH} , M_i , z :

$$\log_{10} f = A + B \log_{10} (\lambda_{RF}/4000\text{\AA}) + C(M_i + 23) + D \log_{10} (M_{BH}/10^9 M_{\odot}) \quad (12)$$

using a Bayesian linear regression method that incorporates measurement uncertainties in all latent variables (Kelly 2007). This ansatz is identical to that used by M10, and very similar to the relation used by Scaringi et al. (2015), since for black holes their Eq.1 becomes $\log t_b = A' \log M_{BH} + B' \log L_{Bol} + C'$ where t_b is the PSD break timescale.

We compare the change in retrieved fit coefficients caused by adding PS1 data to SDSS against M10 SDSS-only study. Note that M10 fitted DRW model treating each of the 5 SDSS bands as a separate light curve, resulting in over thirty thousand values of τ, SF_{∞} for nine thousand S82 quasars. Grouping fitted quasar parameters by band, they were correlated to quasar physical parameters with Eq. 12. Fig. 18 shows the posterior samples for fitting Eq. 12 to $f = SF_{\infty}$ for quasar data separately for each SDSS bandpass. Each band yields a slightly different fit coefficient. M10 reported as the fit result the band-mean (red vertical dashed line). Since this study uses only r band data, we compare the fit coefficients to M10 SDSS r data (green solid vertical line in Fig. 18). We show the results of fitting Eq. 12 to new SDSS and SDSS-PS1 parameters in Figs. 19, 20. First, with $f = \tau$ in Eq. 12 (Fig. 19), the SDSS-PS1 data confirms M10 for luminosity dependence (the posterior MCMC samples overlap), but the dependence of τ on M_{BH} is marginally weaker (by 0.007 dex). Second, in Fig. 20 with $f = SF_{\infty}$, SF_{∞} has a slightly weaker dependence on M_{BH} (by 0.04 dex compared to M10). The difference between *celerite* SDSS-only results and M10 can be attributed to data cleaning that was not performed by M10, and software differences. Each distribution from Figs. 19 and 20 is summarized in Table 2, with the uncertainty in A,C,D fit coefficients estimated from the standard deviation of the posterior samples.

We also searched for signal of Mg II variability (see Cackett et al. 2015 for a review). Mg II, like H α and H β is a permitted low-ionization line (Yang et al. 2019), but

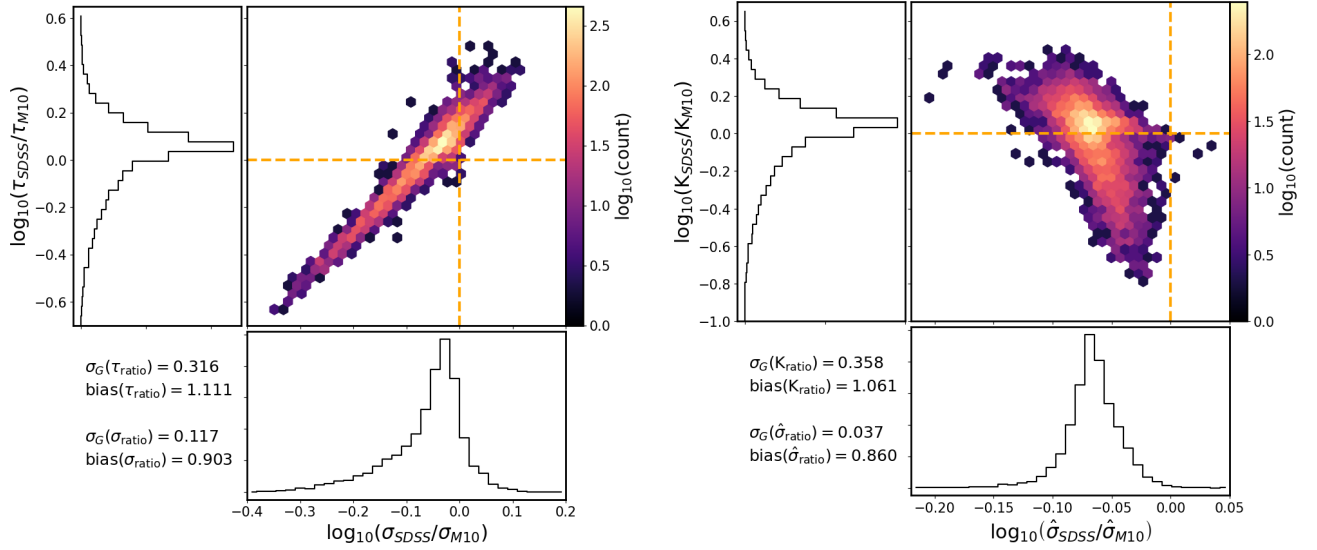


Figure 11. Comparison of celerite fits using only the SDSS r-band segments of S82 quasars ($\sigma_{\text{SDSS}}, \tau_{\text{SDSS}}$), against M10 results for SDSS r-band ($\sigma_{\text{M10}}, \tau_{\text{M10}}$), object-by-object. The small offset (< 0.05 dex) can be attributed to data cleaning and software differences. See Fig. 10 for a comparison of rest-frame τ and SF_{∞} distributions. This is similar to Fig.3 in M10, except we plot only the r-band SDSS results. The right-hand panel shows the comparison in an orthogonal $K - \hat{\sigma}$ space, where K is the direction along the diagonal on the left panel, and $\hat{\sigma}$ -perpendicular to the diagonal. For this reason the right panel has a ten times smaller scatter along $\hat{\sigma}$ (0.037) than K (0.358).

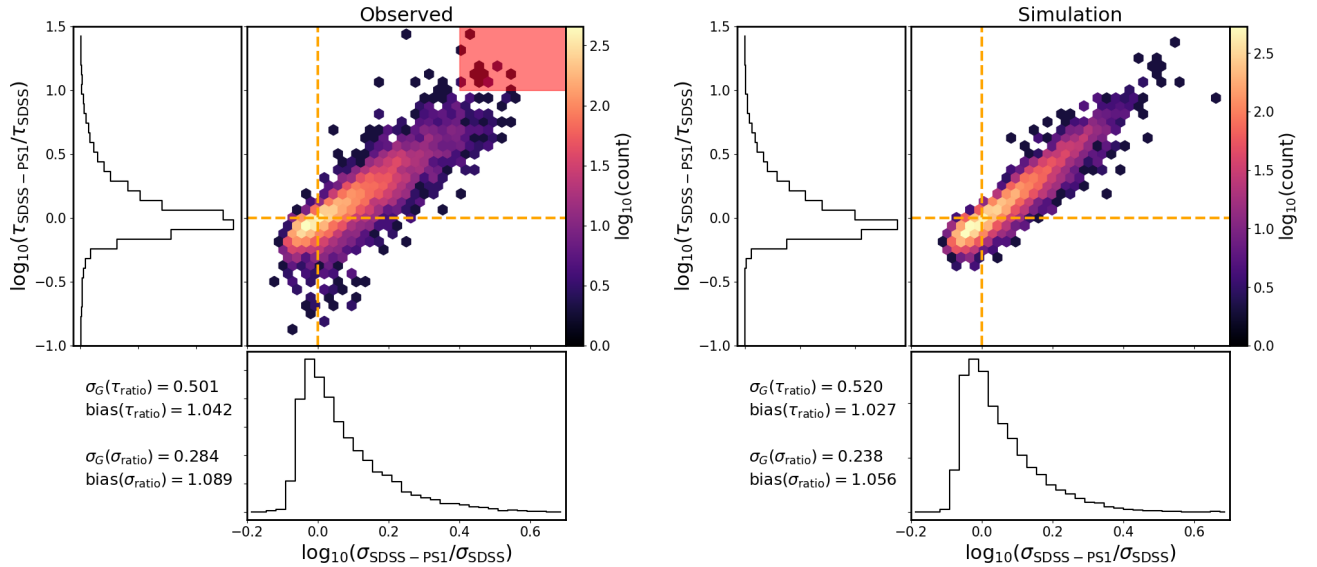


Figure 12. Ratios of fitted DRW parameters (τ, σ), comparing the value of parameter recovered using the combined light curve length (SDSS-PS1) to the shorter, SDSS-only light curve. The left panel shows the results for S82 quasars using real data, whereas the right panel shows the simulated quasars with realistic cadence, with $\tau_{in} = 575$ days and $\text{SF}_{\infty} = 0.2$ (right). The general trend when using the real data (despite having a range of underlying timescales and amplitudes) is similar to that when using simulated data: the diagonal scatter is along the lines of constant $\hat{\sigma}$, and there is much less scatter in the perpendicular direction of K (see Fig. 13). There is no major change of shape of distribution as a function of mean quasar magnitude. The red rectangle marks the outliers with $\log(\tau_{\text{SDSS-PS1}}/\tau_{\text{SDSS}}) > 1$ and $\log(\sigma_{\text{SDSS-PS1}}/\sigma_{\text{SDSS}}) > 0.4$, discussed in Sec. 5.2.

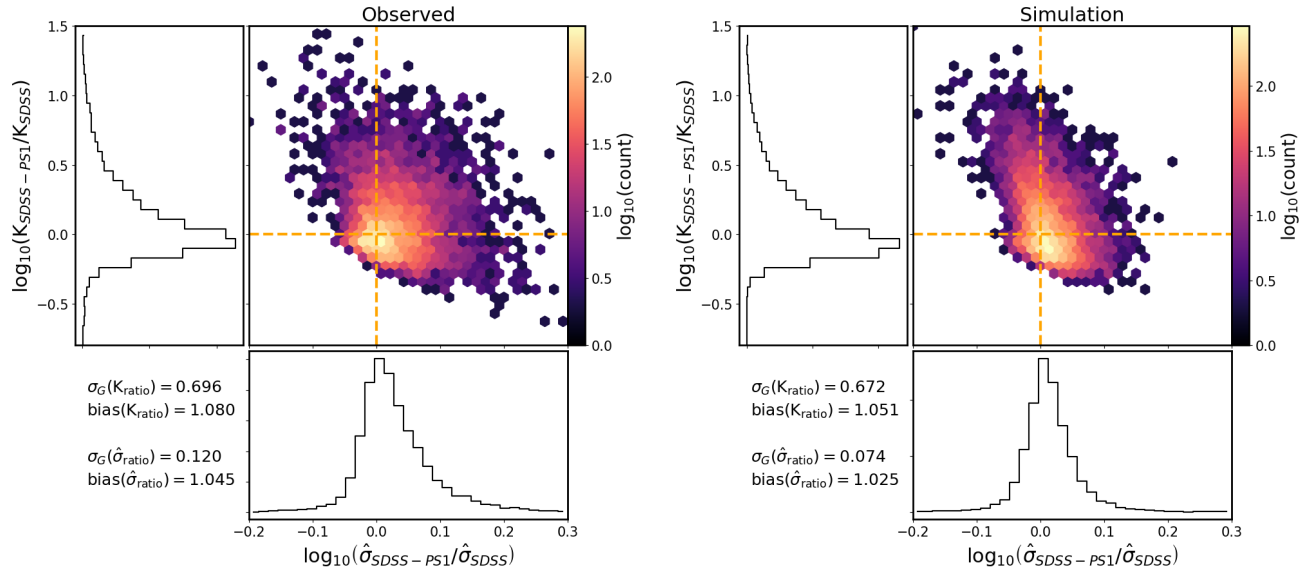


Figure 13. As Fig. 12, but in $K - \hat{\sigma}$ space, which is orthogonal to the $\tau - \sigma$ space, since $K = \tau\sqrt{\text{SF}_\infty} = \tau\sqrt{\sigma}2^{1/4}$ and $\hat{\sigma} = \text{SF}_\infty/\sqrt{\tau} = \sigma\sqrt{2/\tau}$.

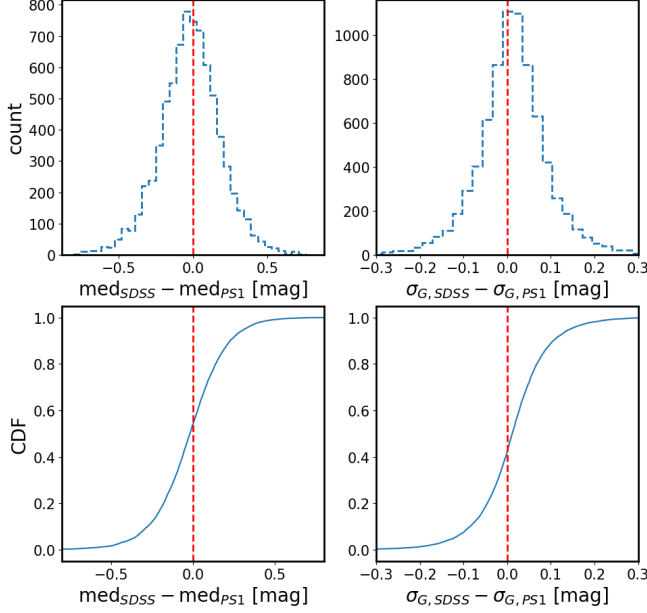


Figure 14. The differences between SDSS and PS1 segments of combined quasar r-band light curves. First, the difference between median SDSS and median PS1 portion, plotted as a histogram (upper-left panel), and cumulative distribution function (lower-left panel). Then, the difference between σ_G calculated for each portion of the light curve (σ_G is a robust estimate of the standard deviation, and is related to the difference between 75th and 25th percentile : $\sigma_G = 0.7413(Q_{75} - Q_{25})$). The outliers in the median offset space are also outliers in the DRW parameter space (eg. objects with $\log(\tau_{\text{SDSS-PS1}}/\tau_{\text{SDSS}}) > 1$ and $\log(\sigma_{\text{SDSS-PS1}}/\sigma_{\text{SDSS}}) > 0.4$) and $r > 20.5$ have $\Delta(\text{median}) > 0.1$).

on average is being emitted by gas further away from the ionizing source than the H β , possibly at the edge of the BLR (Guo et al. 2019). Ivezić et al. (2004) and MacLeod et al. (2012) studied the SDSS-POSS sample of quasars, and report the detection of a decrement in the data-model residuals around 2800 Å when plotting the residuals as a function of Δt and λ_{RF} . We investigated the data-model residuals for $f = \text{SF}_\infty$ in Eq. 12. We find that using the SDSS data the decrement in the median(τ_{RF}) around 2800 Å is visible at $\sim 3\sigma$ relative to the smooth model, but adding the PS1 data the significance rises to $\sim 5\sigma$. We do not see much difference with regards to whether using the subset of 6371 quasars for which M10 had reliable results (listed in Table 2), versus the full set of 8516 quasars fitted with Celerite for DRW parameters. The effect is interesting, but does not produce very significant signal - see Appendix C for more details.

5.5. Comparison to other studies: Eddington ratio

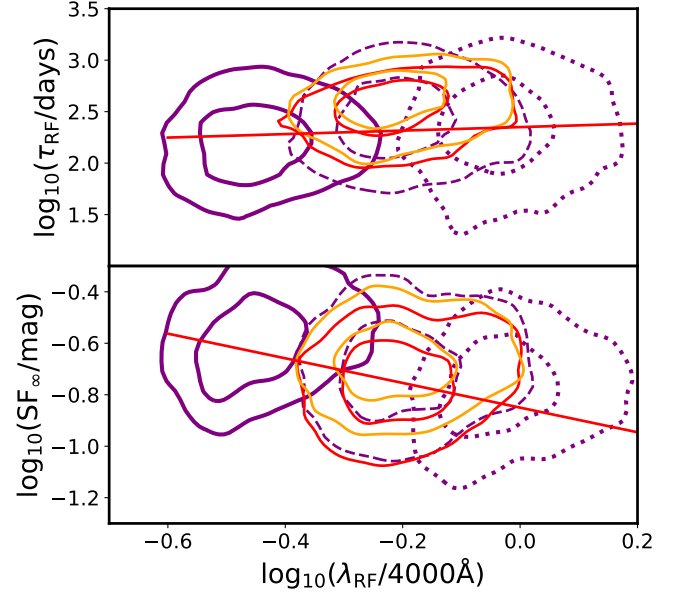


Figure 15. Rest-frame timescale τ (top panel), and asymptotic structure function SF_∞ (bottom panel), as a function of rest-frame wavelength λ_{RF} . The background contours show the 30% and 70% levels for M10 SDSS *urz* data, and the foreground contours denote our results using SDSS (red) and SDSS-PS1 (orange) segments. The red line indicates the best-fit power law to M10 data, with $B = 0.17$ and -0.479 for τ_{RF} , and SF_∞ , respectively. We take the center of each bandpass to approximate the observed wavelength: that is, for SDSS *urz* bandpasses, $\lambda_{\text{obs}} = 3520, 6250, 9110$ Å, respectively, and given the redshift of each quasar, find $\lambda_{\text{RF}} = \lambda_{\text{obs}}/(1+z)$.

Eddington ratio ($f_{\text{Edd}} = L_{\text{Bol}}/L_{\text{Edd}}$) encodes accretion strength: the proximity of quasar bolometric luminosity to the theoretical Eddington limit, where $L_{\text{Edd}} = 1.26 \times 10^{38} (M_{\text{BH}}/M_\odot)$ erg/s (Shen et al. 2011). Since τ and SF_∞ depend on M_i and M_{BH} , we investigate the possibility of the Eddington ratio being the driver of these observed trends. On Fig. 21 we show f_{Edd} as a function of M_i , M_{BH} , and SF_∞ . The left two panels depict f_{Edd} and SF_∞ binned as a function of M_i and M_{BH} . Third panel shows the quasar counts, and the fourth panel the bin means (black dots). The means are further binned along f_{Edd} (as in M10). Combined SDSS-PS1 data supports SF_∞ being inversely related to f_{Edd} , with power-law slope of -0.207 ± 0.03 , consistent with -0.23 ± 0.03 reported by M10. Observations are generally consistent with basic predictions from Table 3: A increases with increasing M_{BH} , and f_{Edd} decreases as L_{Bol} increases, while τ increases with L_{Bol} . No model from Table 3 is rejected.

6. DISCUSSION

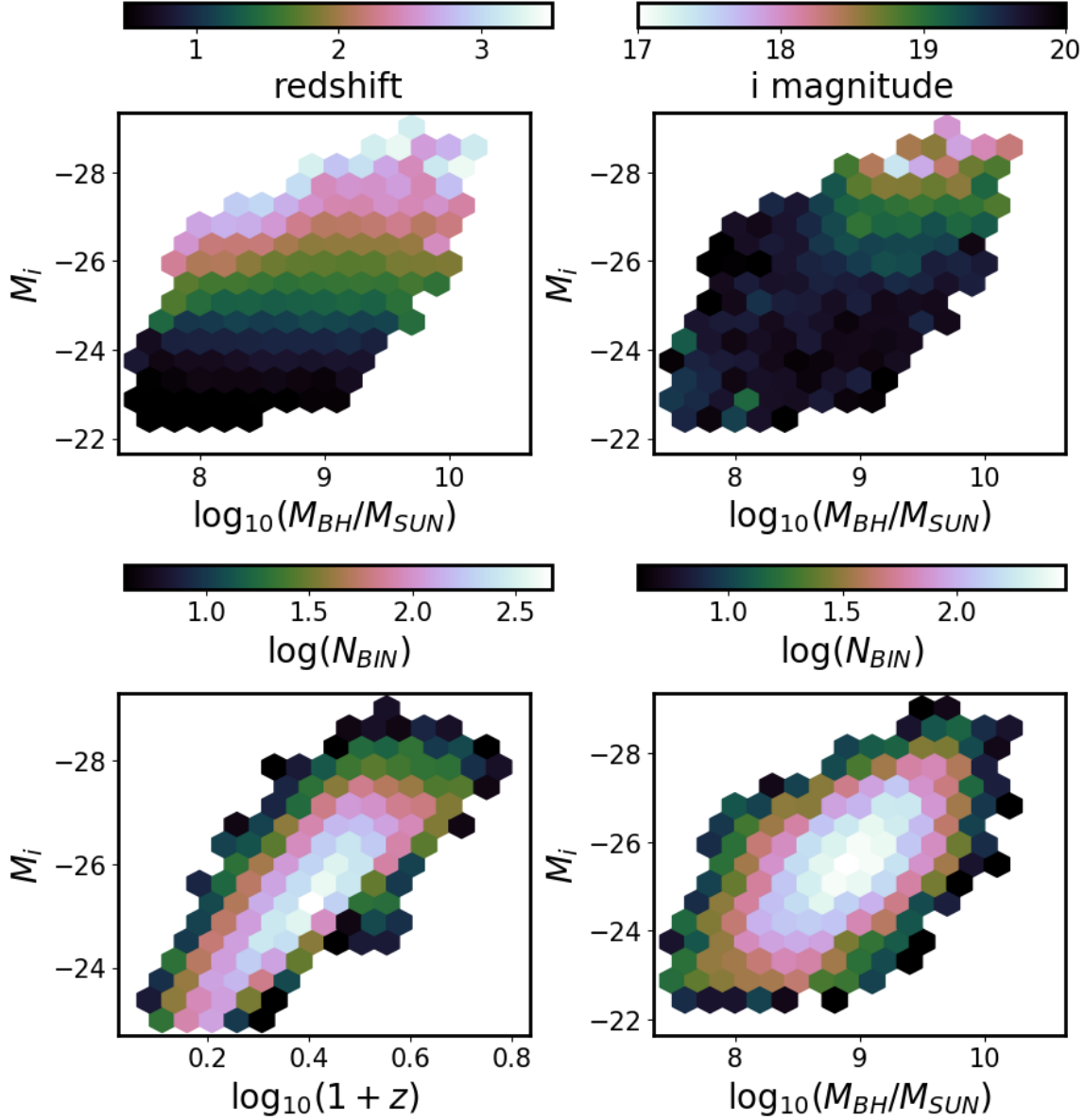


Figure 16. Distribution of quasars as a function of redshift, observed i-band magnitude, absolute i-band magnitude (K-corrected to $z=2$), and virial black hole mass. All data from Shen et al. (2011).

6.1. Trends with Eddington ratio

Anticorrelation of variability amplitude with Eddington ratio has a variety of possible theoretical explanations. In the thin disk theory (Shakura & Sunyaev 1973; Frank et al. 2002; Netzer 2013), radius of the emission region at given wavelength increases with Eddington ratio, and is inversely proportional to temperature (Rakshit & Stalin 2017). Thus a hotter disk means that the emission observed in a given bandpass is emitted from a larger radius. From causality, a smaller region can be more variable than a larger one. Therefore, a hotter disk would be less variable at a given wavelength than a colder one, and the variability amplitude as studied

in a particular bandpass (here, SDSS r-band) would be anticorrelated with Eddington ratio (Fausnaugh et al. 2016; Edelson et al. 2015).

On the other hand, in the strongly inhomogeneous disk model independent temperature fluctuations in N zones drive the variability (Dexter & Agol 2011). In that framework the inverse trend of variability amplitude against L/L_{Edd} and L_{Bol} can be understood qualitatively if more luminous quasars also have higher mass accretion rate, and thus greater number of disk inhomogeneities, resulting in smaller flux variability (Simm et al. 2016). The inhomogeneous disk model was consistent with mean SDSS spectral analysis in Ruan et al.

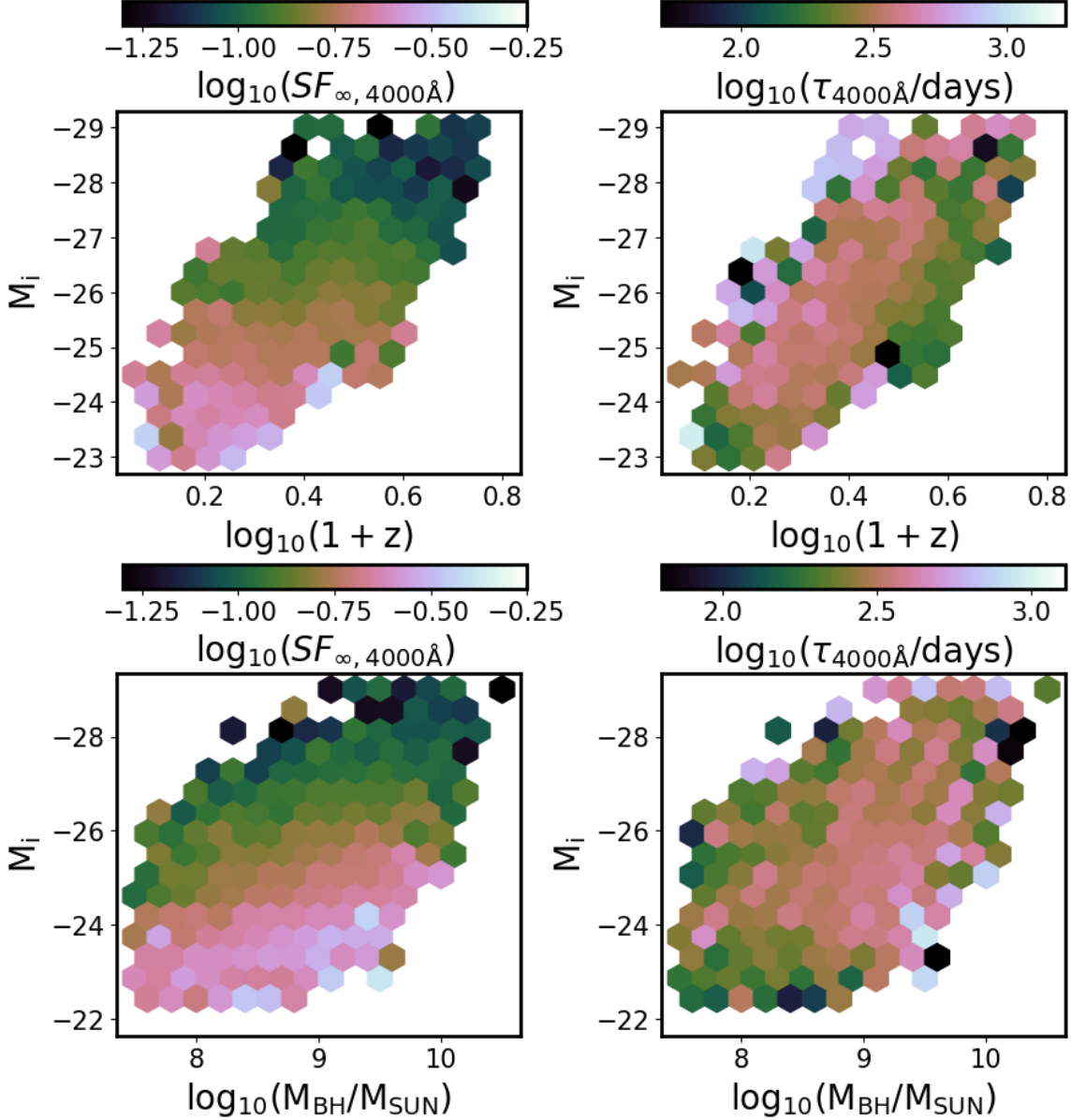


Figure 17. The absolute i-band magnitude M_i (k-corrected to $z = 2$) as a function of the virial black hole mass M_{BH} (bottom panels) and redshift z (top panels), colored by the long-term variability amplitude SF_{∞} (left panels), or characteristic timescale τ (right panels). M_i is a proxy for quasar bolometric luminosity, and the DRW variability parameters are for combined SDSS-PS1 r -band data.

(2014), but was not a preferred explanation for Kokubo (2015).

Both Rumbaugh et al. (2018) (with Dark Energy Survey structure function study) and Sun et al. (2018) (with a low- z subsample of S82 SDSS quasars) confirm the anti-correlation between quasar variability and luminosity. However, Graham et al. (2019) do not find support for this trend with the sample of extremely variable quasars (EVQs) in the CRTS dataset, but when selecting for lower luminosity sources ($M_V < -23$), the anti-correlation is recovered. This agrees with an inter-

pretation that a dwindling fuel supply may correspond to higher variability. Furthermore, Sánchez-Sáez et al. (2018) combined the SDSS spectra with 5 year light curves of 2345 quasars obtained with Quasar Equatorial Survey Team (QUEST)-La Silla AGN Variability Survey, and using the Bayesian parametrization of Structure Function (Schmidt et al. 2010) they also found that the amplitude of variability A is anti-correlated with rest-frame emission wavelength, and Eddington ratio (also see Simm et al. 2016, Rakshit & Stalin 2017).

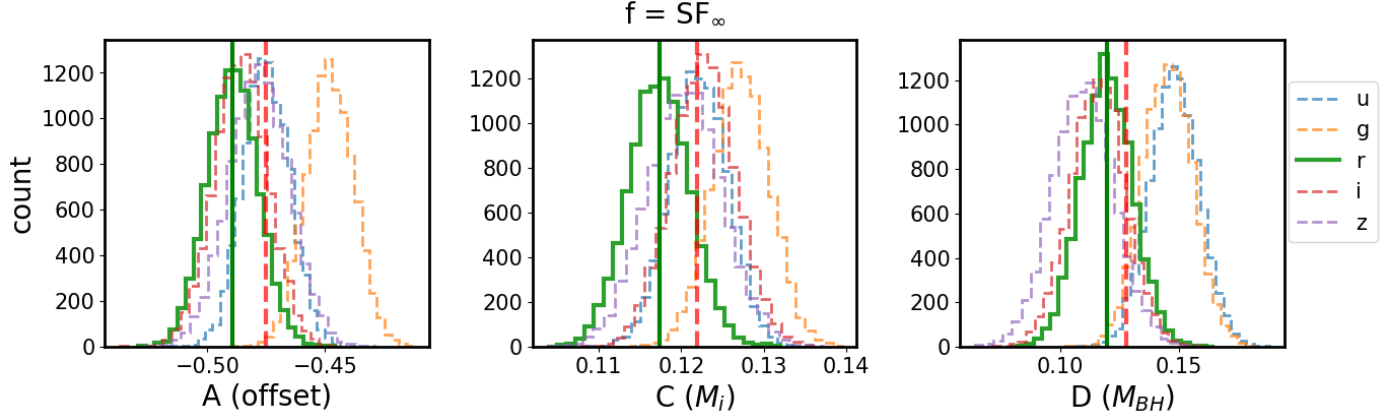


Figure 18. Posterior MCMC draws for fitting Eq. 12 with M10 variability amplitude SF_∞ against M_{BH} , M_i , z (Shen et al. 2011). Since M10 treated the near-simultaneous SDSS *ugriz* data for 9258 quasars, independently for each band, this resulted in DRW fit parameters for 7014 *u*, 7408 *g*, 6871 *r*, 6814 *i*, and 5111 *z*-band SDSS quasar light curves that fulfilled M10 quality of DRW fit selection criteria. M10 values for SF_∞ are corrected to 4000 Å using Eq. 11, with the power-law coefficient $B = -0.479$. Each distribution corresponds to a different SDSS band. We compare the results of fitting SDSS-PS1 *r*-band directly against M10 results for SDSS *r*-band (solid green). Note that Table 1 in M10 reported band-averaged values for A,C,D coefficients (vertical dashed red line), while we cite in Table 2 the mean for *r*-band (vertical solid green line).

Table 2. Comparison of best-fit coefficients for Eq. 12 using M10 results, and this work (S20). B is fixed to 0.17 or -0.479 from fitting a power law between λ_{RF} and τ , SF_∞ (see Fig. 15). Of 8516 quasars with SDSS-PS1 data, for consistency we use here an unbiased subset of 6371 quasars for which M10 had reliable results. For $f = \tau$, C is almost the same between M10 and this work for SDSS-PS1 (rows 1 and 3). However, D based on SDSS-PS1 data is larger than M10 by 0.01 dex (row 3). For $f = SF_\infty$, SDSS-PS1 based C is within 0.01 dex from M10 (rows 4,6), and D based on SDSS-PS1 data is almost identical to M10. When using *celerite* τ (σ) results for all 8516 quasars, the luminosity dependence is unchanged to within 0.01 dex, and the dependence on the black hole mass is stronger by 0.05 dex (0.02 dex), respectively. **As shown on Fig. 11, there is a small offset between $\log_{10}(\tau_{S20,SDSS}/\tau_{M10,SDSS})$ and $\log_{10}(\sigma_{S20,SDSS}/\sigma_{M10,SDSS})$, attributed to data cleaning procedures and software differences, which contributes to a shift between C and D parameters for τ and SF_∞ between M10 and S20.**

f	Source	$A(\text{offset})$	$B(\lambda_{RF})$	$C(M_i)$	$D(M_{BH})$
τ	M10, SDSS	2.5 ± 0.027	0.17 ± 0.02	0.03 ± 0.009	0.178 ± 0.027
	S20, SDSS	2.515 ± 0.019	0.17 ± 0.02	0.042 ± 0.007	0.127 ± 0.019
	S20, SDSS-PS1	2.597 ± 0.02	0.17 ± 0.02	0.035 ± 0.007	0.141 ± 0.02
SF_∞	M10, SDSS	-0.486 ± 0.012	-0.479 ± 0.005	0.119 ± 0.004	0.121 ± 0.012
	S20, SDSS	-0.543 ± 0.009	-0.479 ± 0.005	0.125 ± 0.003	0.104 ± 0.008
	S20, SDSS-PS1	-0.476 ± 0.008	-0.479 ± 0.005	0.118 ± 0.003	0.118 ± 0.008

Indeed, f_{Edd} is a proxy for the strength of accretion, which together with orientation may be the key to explaining quasar main sequence (QMS: Shen & Ho 2014; Marziani et al. 2018). The QMS, defined by so-called Eigenvector-1, is the anti-correlation between the broad line FeII emission, and the strength of the narrow OIII (5007 Å) line (Wang et al. 1996). An analysis of quasar clustering by Shen & Ho (2014), later confirmed by Sun

& Shen (2015) with measurements of black hole mass from the quasar host galaxy stellar dispersion (Ferrarese & Merritt 2000; Kormendy & Ho 2013), showed that the entire diversity of quasars in QMS can be explained by the variation in accretion (affecting R_{FeII} - the ratio of the FeII EQ between 4435 – 4685 Å and H β), or orientation effects (affecting the FWHM of the H β). However, Panda et al. (2019a,b) found that these are insuf-

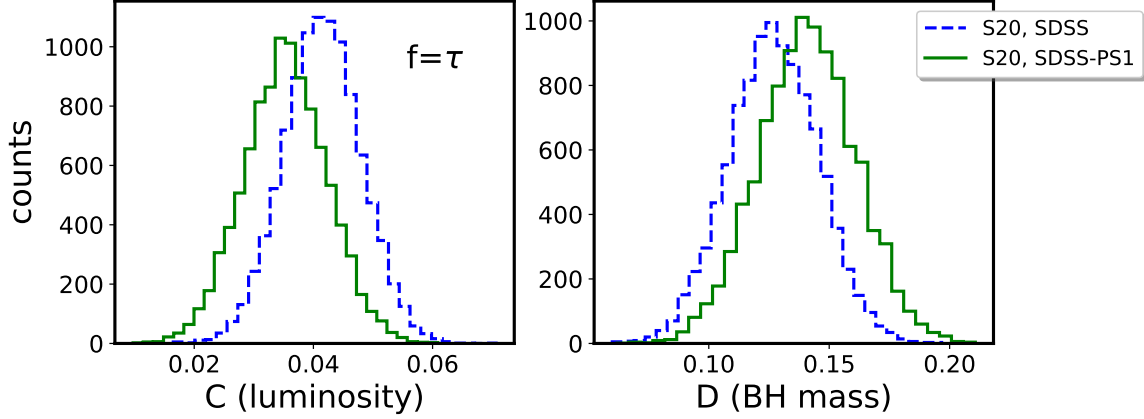


Figure 19. Distribution of MCMC posterior draws fitting Eq. 12 for characteristic timescale ($f = \tau$), based SDSS r -band results (dashed blue line), and new SDSS-PS1 combined r -band results (solid blue line). These are considered simultaneously as a function of quasar absolute magnitude M_i (left hand side panel), and black hole mass M_{BH} (right hand side panel). Of 9258 spectroscopically confirmed quasars in S82, we employed 8516 that had PS1 matches, of which 6371 fulfill M10 selection criteria (see M10, Sec 2.2). The results from SDSS-PS1 light curves are consistent with M10 for the SDSS r band.

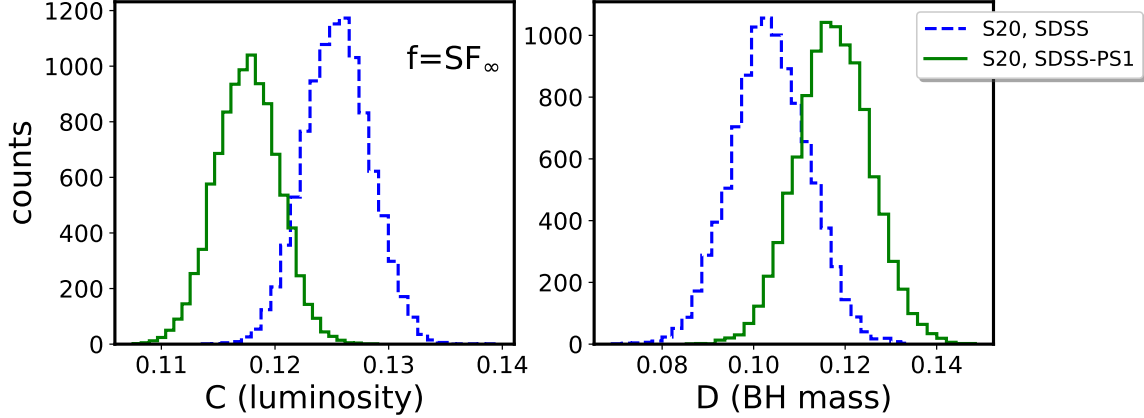


Figure 20. Same as Fig. 19, but fitting the DRW asymptotic amplitude ($f = SF_\infty$ in Eq. 12) as a function of absolute magnitude M_i , and black hole mass M_{BH} . New data from PS1 is consistent with earlier results of M10 on luminosity dependence, but supports slightly weaker dependence of SF_∞ on M_{BH} (by 0.06 dex).

Table 3. Theoretical predictions of various models concerning amplitude A and/or timescale τ of variability, Eddington ratio f_{Edd} , bolometric luminosity L_{Bol} , and accretion rate \dot{m} . Observations cannot reject any model.

Theory	Prediction
Standard thin disk (Shakura & Sunyaev 1973; Netzer 2013)	$A \nearrow$ as $f_{Edd} \searrow$, $\tau \propto L_{Bol}^{1/2}$ (in Caplar et al. 2017)
Strongly inhomogeneous disk (Dexter & Agol 2011) / local fluctuations (Cai et al. 2018)	$A \nearrow$ as $f_{Edd} \searrow$
Variations in global accretion rate (Hawkins 2007; Li & Cao 2008; Zuo et al. 2012)	$A \nearrow$ as $M_{BH} \nearrow$, $A \searrow$ as $L_{Bol} \nearrow$
Eddington ratio reflecting AGN age (Martini & Schneider 2003; Hopkins et al. 2005)	$A \nearrow$ as $f_{Edd} \searrow$
X-ray reprocessing (Kubota & Done 2018)	$A \nearrow$ as $f_{Edd} \searrow$, and $A \nearrow$ as $\dot{m} \searrow$

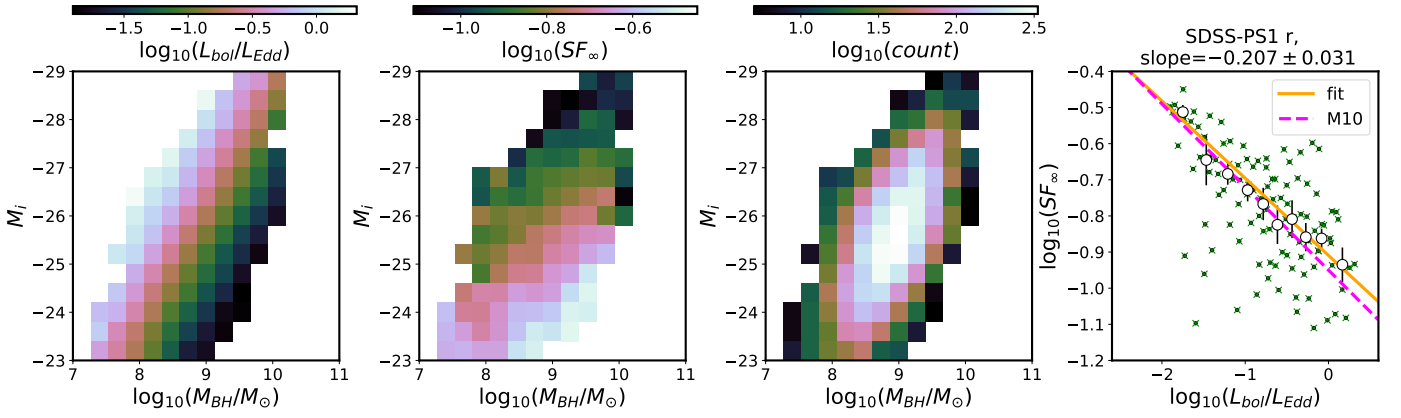


Figure 21. Absolute i-band magnitude M_i as a function of black hole mass M_{BH} , where color encodes Eddington ratio $f_{Edd} = L/L_{Edd}$ (first panel), variability amplitude SF_∞ (second panel), or quasar count (third panel). We only plot bins with more than five quasars. The fourth panel shows median SF_∞ as a function of median f_{Edd} (green crosses), averaged in bins of f_{Edd} (open circles). The bin width w is found to ensure equal number of points (crosses) per bin (N). The error bars are $\sigma_y = 1.25\sigma_G(\text{bin})/N$, where σ_G is the robust estimate of the standard deviation ($\sigma_G = 0.7413(Q_{75} - Q_{25})$). We assume the uncertainty along f_{Edd} as $\sigma_x = w/\sqrt{12}$ (see Ivezić et al. 2014). The solid orange line is the best-fit slope: -0.207 ± 0.031 , with the slope uncertainty estimated from the standard deviation of the posterior samples. The best-fit slope agrees with M10 results (-0.23 ± 0.03), plotted as dashed magenta line.

Table 4. Comparison of published results on correlating observed quasar light curve properties: a measure of variability amplitude A , and timescale of variability τ , against the physical quasar properties: Black Hole mass M_{BH} , Eddington ratio f_{Edd} , bolometric luminosity L_{Bol} . We list the correlations as positive (+), negative (−, i.e. anti-correlation), not found (0), or not studied (x). We further note if the correlation is strong (!), or weak (\sim).

Publication	Measure of amplitude / timescale	A vs			τ vs		
		M_{BH}	f_{Edd}	L_{Bol}	M_{BH}	f_{Edd}	L_{Bol}
Wilhite et al. (2008)	SF (ensemble study)	+	−	−	x	x	x
Kelly et al. (2009)	DRW: τ -decorrelation timescale, σ	−	0	!−	+	x	\sim +
MacLeod et al. (2010)	DRW: τ, σ	+	!−	!−	+	x	\sim +
Morganson et al. (2014) ^a	SF: A, γ	x	x	−	x	x	+
Kozłowski et al. (2016)	DRW: τ, σ	x	x	!−	+	x	\sim +
Simm et al. (2016) ^b	EV, and PSD (break timescale)	0	−	−	0	0	0
Caplar et al. (2017)	SF: τ, σ	\sim	x	!−	x	x	+
Rakshit & Stalin (2017) ^c	DRW: τ, σ	+	!−	\sim +	x	x	x
Sun et al. (2018) ^d	SF: τ, σ	x	x	!−	x	+	!+
Li et al. (2018) ^e	SF: A, γ	\sim +	−	−	+	x	+
Sánchez-Sáez et al. (2018) ^f	SF: A	0	−	x	x	x	x
This work	DRW: τ -decorrelation timescale, σ	+	!−	+	+	x	\sim +

^a 105 783 quasars with SDSS-PS1 sparse data, SF parametrized as $V(\Delta t|A, \gamma) = A(\Delta t/1\text{year})^\gamma$: γ is the increase of SF with time lag Δt

^b 90 X-ray selected AGN, PS1 optical data. Variability characterized by normalized excess variance (EV). PSD characterized by break timescale.

^c Narrow- and Broad-Line Seyfert1 AGN, $z < 0.8$, CRTS data (> 50 epochs, 5 – 9 years baseline), DRW fitted with JAVELIN (Zu et al. 2011), no timescale correlations considered due to short baseline.

^d 1004 SDSS quasars with $0.5 \leq z \leq 0.89$

^e 119 305 sparse quasar light curves from DECaLS and SDSS. SF as in Morganson et al. (2014) above.

^f 1348 QUEST-La Silla quasars, only amplitude of variability and excess variance.

ficient, and variations in metallicity, as well as a range of cloud densities, and turbulences are required. Jiang et al. (2016) also found that metallicity, and in particular the iron opacity bump, may have a strong influence on the stability of an accretion disk, and thus linking metallicity to AGN variability. This is also consistent with findings of Sun et al. (2018): quasars with high FeII strength have higher metallicity, and have more stable disks.

6.2. Variability Timescales

In the era of changing-look active galaxies (including initially distinct classes of Changing-Look Quasars (LaMassa et al. 2015; MacLeod et al. 2019), Changing-Look AGNs (Marchese et al. 2012; Bianchi et al. 2009; Risaliti et al. 2009), Changing-Look LINERS (Frederick et al. 2019) to name a few) there is a revived interest in possibly linking the behavior of stellar-sized accreting systems (eg. Black Hole Binaries), to that of galactic

scale (eg. AGN, QSO, LINERS - Noda & Done 2018; Ruan et al. 2019).

Several relevant timescales are involved, and there are various interlinked mechanisms that could drive the variability. A standard optically thick, geometrically thin, α -disk model has a hierarchy of timescales: dynamical, thermal, front, viscous, with $t_{\text{dyn}} < t_{\text{th}} < t_{\text{front}} < t_{\text{visc}}$ (Netzer 2013; Frank et al. 2002). We proceed to describe briefly each timescale, concluding with our interpretation of the mechanism that could drive the variability observed from the data.

The dynamical, or gas orbital, timescale is simply an inverse of the Keplerian orbital angular frequency Ω at radius R :

$$t_{\text{dyn}} \sim 1/\Omega = \left(\frac{GM}{R^3} \right)^{-1/2} \quad (13)$$

The main parameter describing the accretion disk is α - the ratio of the (vertically averaged) total stress to thermal (vertically averaged) pressure:

$$\alpha = \frac{\langle \tau_{r\varphi} \rangle_z}{\langle P \rangle_z} \quad (14)$$

After Lasota (2016), the hydrodynamical stress tensor (corresponding to kinematic viscosity ν) is:

$$\tau_{r\varphi} = \rho \nu \frac{\partial v_\varphi}{\partial R} = \rho \nu \frac{d\Omega}{d \ln R} = \frac{3\rho \nu \Omega}{2} \quad (15)$$

so with c_s - local sound speed at radius R (isothermal sound speed is $c_s = \sqrt{P/\rho}$),

$$\alpha = \frac{3\rho \nu \Omega}{2P} = \frac{3\Omega \nu}{2c_s^2} \quad (16)$$

This means that smaller α corresponds to less viscous disks.

The thermal timescale, related to the time needed for re-adjustment to the thermal equilibrium (derived in detail in Frank et al. 2002), is the ratio of heat content per unit disk area to dissipation rate per unit disk area: $(dE/A)/(dE/dt/A) = dt$. The heat content per unit volume is $\sim \rho kT/\mu m_p \sim \rho c_s^2$, and heat content per unit area is $\sim \rho c_s^2 h \sim \Sigma c_s^2$. Meanwhile, the dissipation rate per unit area, $D(R)$, is

$$D(R) = \frac{9}{8} \nu \Sigma R^{-3} GM \quad (17)$$

(eq. 4.30 in Frank et al. 2002), so :

$$t_{th} \sim \frac{c_s^2 R^3}{GM \nu} = \frac{c_s^2}{\nu \Omega} = \frac{t_{dyn}}{\alpha} \quad (18)$$

Thus if the disk were inviscid ($\nu \rightarrow 0$), then $t_{th} \rightarrow \infty$ i.e. there is no contact with adjacent disk elements.

The cooling and heating fronts propagate through the disk at αc_s (Hameury et al. 2009) - in that description with no viscosity there is no communication between neighboring disk annuli, and thus no front propagation (Balbus & Hawley 1998; Balbus 2003). Following Stern et al. (2018), if we define as h/R the the disk aspect ratio, with the disk height $h = c_s/\Omega$, the characteristic time for front propagation is:

$$t_{front} \sim (h/R)^{-1} t_{th} \quad (19)$$

The viscous timescale is the characteristic time it would take for a parcel of material to undergo a radial transport due to the viscous torques from the radius R to the black hole (Czerny 2006). Note that while viscosity has probably magnetic origin (Eardley & Lightman 1975; Grzędziński et al. 2017), in this simplistic order

of magnitude estimate we use a hydrodynamical description of accretion flow. With $\nu = \eta/\rho$ (kinematic viscosity being the ratio of dynamical viscosity to density), Frank et al. (2002) shows (Chap.5.2) that

$$t_{visc} \sim R^2/\nu \sim R/v_R = (h/R)^{-2} t_{th} \quad (20)$$

We can parametrize each timescale for a black hole mass $M_{BH} = 10^8 M_\odot$, at $R \sim 150 r_g$, with the gravitational radius $r_g = GM_{BH}/c^2 \sim 4 \text{ au}$, using Eqs.5-8 in Stern et al. (2018) :

$$t_{dyn} \sim 10 \text{ days} \left(\frac{M_{BH}}{10^8 M_\odot} \right) \left(\frac{R}{150 r_g} \right)^{3/2} \quad (21)$$

$$t_{th} \sim 1 \text{ year} \left(\frac{\alpha}{0.03} \right)^{-1} \left(\frac{M_{BH}}{10^8 M_\odot} \right) \left(\frac{R}{150 r_g} \right)^{3/2} \quad (22)$$

$$t_{front} \sim 20 \text{ years} \left(\frac{h/R}{0.05} \right)^{-1} \left(\frac{\alpha}{0.03} \right)^{-1} \left(\frac{M_{BH}}{10^8 M_\odot} \right) \left(\frac{R}{150 r_g} \right)^{3/2} \quad (23)$$

$$t_{visc} \sim 400 \text{ years} \left(\frac{h/R}{0.05} \right)^{-2} \left(\frac{\alpha}{0.03} \right)^{-1} \left(\frac{M_{BH}}{10^8 M_\odot} \right) \left(\frac{R}{150 r_g} \right)^{3/2} \quad (24)$$

In summary, of considered timescales only thermal and dynamical are short enough to be related to the observed short-term stochastic variability. It may be that the variability on the scale of days is driven by local changes, and on the longer scale (perhaps hundreds of days) by a different mechanism (Kokubo 2015). The other time scales may be more related to the dramatic changes in brightness of the continuum as observed in changing-look AGN. Indeed, Noda & Done (2018) favor a change in mass accretion rate, followed by a propagation of the cooling front (Lawrence 2018; Simm et al. 2016). Noda & Done (2018) also suggest that perhaps some short-term variability could be related to the amount of the disk swept by the thermal front propagation due to Hydrogen ionization instability, similarly to white dwarf systems (also, see Ruan et al. 2019; Ross et al. 2018; Śniegowska & Czerny 2019).

The variability on several years timescale could also be explained by the X-ray reprocessing model (Kokubo 2015; Kubota & Done 2018), assuming that the AGN UV-optical variability is a result of reprocessing of X-ray or far-UV emission (Krolik et al. 1991). The idea of

X-ray reprocessing over time has gained more and more support, with evidence from simultaneous X-ray-UV-optical AGN time series (Edelson et al. 2014; McHardy et al. 2018; Zhu et al. 2018). In particular, the accretion disk blackbody emission is insufficient to explain the broadband AGN spectrum. The total SED with a soft X-ray excess, and a hard X-ray tail, requires additional sources of emission. A recent model by Kubota & Done (2018) divides the flow into blackbody emission, warm Comptonization region (the disk), and hard X-ray hot Comptonization component (corona, or a hot material filling the region close to the black hole below the truncation radius). Since the soft X-rays are correlated with the hard X-rays, at least part of the picture consists of reflection or reprocessing of hard X-rays by the disk (Lawrence 2018). This model predicts an increase of variability amplitude (SF_{∞}) with M_{BH} , and adds an insight that the observed slope is due to changes in accretion rate \dot{m} , explaining that smaller \dot{m} corresponds to highest variability. This qualitatively agrees with the picture that dwindling fuel supply makes the flow more variable. Previous worries about X-ray reprocessing concerned the seemingly insufficient solid angle subtended by the source of the hard X-rays to cause the observed soft X-ray and optical response. This is addressed by realizing that reprocessing could be taking place in the extended region (Gardner & Done 2017), such as an inflated inner disk (corresponding to warm Comptonizing region in Kubota & Done 2018, or even the BLR region serving as an additional ‘complex reprocessor’ (McHardy et al. 2018). Also, for Panda et al. (2019a) warm corona helps decrease the dependence of R_{FeII} on f_{Edd} .

Thus while CLAGN may be related to the state-change to ADAF flow (Śniegowska & Czerny 2019), similar to that of XRBs (Noda & Done 2018; Ruan et al. 2019), with cooling and heating fronts (Ross et al. 2018), the short-timescale variability requires approximately three distinct emission regions (Kubota & Done 2018), with extended reprocessor (such as diffuse, hot, puffed-up inner disk, and BLR - McHardy et al. 2018), that reverberates the rapid hard X-ray variability in soft X-rays to optical via UV (Fausnaugh et al. 2018). Some emission (especially soft X-rays) seems to require the warm Comptonizing corona (Kubota & Done 2018). The warm corona, coupled with metallicity changes, and variation in turbulence level and cloud density, also helps explain the Quasar Main Sequence in the optical (Panda et al. 2019a,b). Finally, the Kubota & Done (2018) model, apart from being consistent with other mechanisms (McHardy et al. 2018; Panda et al. 2019a; Śniegowska & Czerny 2019; Lawrence 2018; Ross et al.

2018; Ruan et al. 2019), explains the observed correlation of variability amplitude with black hole mass as corresponding to variations in mass accretion rate.

7. SUMMARY AND CONCLUSIONS

We model the optical variability of ~ 9000 Stripe 82 quasars as the Damped Random Walk (DRW, Kelly et al. 2009). DRW is a Gaussian Process (GP), described by two parameters - characteristic timescale τ (representing decorrelation timescale, or light curve smoothness), and the asymptotic amplitude SF_{∞} (which relates to the amplitude of variability). We fit observed and simulated light curves with *celerite* - a fast GP solver (Foreman-Mackey et al. 2017). By simulating and fitting DRW light curves, we explore the impact of the ratio of input timescale and the light curve baseline. We find that the light curve length needs to be several **times** larger than input timescale to allow unbiased timescale retrieval, confirming K17. Motivated by this result we consider extending SDSS with PS1, PTF, CRTS, and ZTF data. We calculated appropriate photometric offsets (color terms) to relate PS1 gri, PTF gR, CRTS V, and ZTF r to SDSS r-band. However, due to larger photometric uncertainties of PTF, ZTF, CRTS at faint magnitudes of SDSS quasars, we decided to use only PS1 r-band data. Furthermore, SDSS r-band and PS1 r-band are sufficiently similar that no photometric transformation is required. Thus by extending the SDSS r-band light curves with PS1 DR2 r-band data we improve on the fidelity of recovered DRW parameters.

We identify 40 objects which exhibit tenfold increase in variability timescale when using the SDSS-PS1 dataset as compared to timescale inferred from SDSS alone. Their light curves show characteristics of changing-look quasars (magnitude difference larger than 0.5 mag, MacLeod et al. 2016). Of these, 5 are confirmed in the literature (MacLeod et al. 2019; LaMassa et al. 2015). We recommend spectroscopic follow-up and further monitoring of the brightest targets (see Appendix B).

We investigate the correlation of quasar physical properties, such as black hole mass M_{BH} and absolute i-band magnitude M_i , with DRW model parameters. The SDSS-PS1 data, coupled with Shen et al. (2011) quasar catalog, imply that the damping timescale τ is correlated with M_{BH} with a power-law index of 0.141 ± 0.019 , and almost independent of quasar bolometric luminosity, as in M10, Wilhite et al. (2008), and Vanden Berk et al. (2004). The asymptotic variability amplitude SF_{∞} is anti-correlated with luminosity M_i with power law index 0.118 ± 0.003 , and correlated with M_{BH} with slope 0.118 ± 0.008 . This can be explained if the driving vari-

able was Eddington ratio f_{Edd} (Wilhite et al. 2008). Indeed, there is an anti-correlation of SF_∞ and f_{Edd} , with power law slope of -0.207 ± 0.031 (similar to M10). As suggested by Kubota & Done (2018), this gradient of SF_∞ in the plane of M_{BH} vs M_i could be explained if the lower mass accretion rate corresponds to higher variability, so that when the supply of fuel decreases, the flow becomes less stable, more clumpy, and more inhomogeneous (Rakshit & Stalin 2017; Kokubo 2015; Dexter & Agol 2011). This is also consistent with the X-ray reprocessing model, whereby the hard X-ray variability of the inner disk is reflected/reprocessed by the extended warm Comptonization region (inflated disk), and perhaps a complex reprocessor, including the clouds of the broad line region (Kubota & Done 2018; Panda et al. 2019b). Changes on recovered timescales are too fast to be driven by changes in disk viscosity, or thermal front propagation alone - thermal or dynamical timescale of response to the changes in X-ray emission seems most consistent with our results (Stern et al. 2018).

More data extending the light curves would help improve the DRW fit coefficients, potentially decreasing the scatter in observed correlations. Moreover, given that the uncertainty in black hole mass is one of the biggest sources of error, better measurements of quasar properties would be of high utility (Shen et al. 2011). This will be possible by the upcoming AGN reverberation mapping campaigns (eg. SDSS-V Black Hole Mapper), providing better calibration for line width-based methods of estimating black hole masses (Kollmeier et al. 2017). All quasars in this study were spectroscopically confirmed, but some spectra had low signal-to-noise, resulting in higher likelihood of incorrect redshift measurement. Better spectroscopy and follow up of S82 quasars, afforded by SDSS-V panoptic spectroscopy, would not only help improve on the spectrum-based properties (redshift, absolute magnitude, black hole masses), but also allow to study spectral changes, and further new CLAGN discoveries (MacLeod et al. 2019).

If this study were to be expanded onto a sample of quasars with good photometry over sufficiently long baselines, but lacking spectral information, the required physical information on quasars could be obtained by indirect methods of estimating the coarse spectral information from broad-band photometry (Kozłowski 2015). This would benefit from better catalogs of existing spectroscopically-confirmed quasars (SDSS DR14) to improve the calibration, as well as better methods of estimating the redshift based on photometry alone (eg. photo-z: Jin et al. 2019; Curran & Moss 2019; Yang et al. 2017; Richards et al. 2015). This will be possible

in short term with the ZTF (Bellm et al. 2019), and in the long term with LSST (Ivezić et al. 2019). Occasional coverage adding few epochs to some quasars may be possible with other surveys (eg. TESS, Ricker et al. 2014), but to improve the statistics of an entire sample of S82 quasars would require longer baselines. Combining SDSS and PS1 with LSST would provide unprecedented 35-year baseline, which assuming timescales below 1000 days is over 10 times longer, allowing unbiased DRW parameter retrieval, which coupled with correlations with quasar properties, would provide an estimate of black hole masses and bolometric luminosities for millions of quasars (Ivezić et al. 2019).

8. ACKNOWLEDGMENTS

The Pan-STARRS1 Surveys (PS1) and the PS1 public science archive have been made possible through contributions by the Institute for Astronomy, the University of Hawaii, the Pan-STARRS Project Office, the Max-Planck Society and its participating institutes, the Max Planck Institute for Astronomy, Heidelberg and the Max Planck Institute for Extraterrestrial Physics, Garching, The Johns Hopkins University, Durham University, the University of Edinburgh, the Queen's University Belfast, the Harvard-Smithsonian Center for Astrophysics, the Las Cumbres Observatory Global Telescope Network Incorporated, the National Central University of Taiwan, the Space Telescope Science Institute, the National Aeronautics and Space Administration under Grant No. NNX08AR22G issued through the Planetary Science Division of the NASA Science Mission Directorate, the National Science Foundation Grant No. AST-1238877, the University of Maryland, Eotvos Lorand University (ELTE), the Los Alamos National Laboratory, and the Gordon and Betty Moore Foundation.

Funding for the Sloan Digital Sky Survey IV has been provided by the Alfred P. Sloan Foundation, the U.S. Department of Energy Office of Science, and the Participating Institutions. SDSS-IV acknowledges support and resources from the Center for High-Performance Computing at the University of Utah. The SDSS web site is www.sdss.org. SDSS-IV is managed by the Astrophysical Research Consortium for the Participating Institutions of the SDSS Collaboration including the Brazilian Participation Group, the Carnegie Institution for Science, Carnegie Mellon University, the Chilean Participation Group, the French Participation Group, Harvard-Smithsonian Center for Astrophysics, Instituto de Astrofísica de Canarias, The Johns Hopkins University, Kavli Institute for the Physics and Mathematics of the Universe (IPMU) / University of Tokyo, the Korean Participation Group, Lawrence Berkeley National

Laboratory, Leibniz Institut für Astrophysik Potsdam (AIP), Max-Planck-Institut für Astronomie (MPIA Heidelberg), Max-Planck-Institut für Astrophysik (MPA Garching), Max-Planck-Institut für Extraterrestrische Physik (MPE), National Astronomical Observatories of China, New Mexico State University, New York University, University of Notre Dame, Observatório Nacional / MCTI, The Ohio State University, Pennsylvania State University, Shanghai Astronomical Observatory, United Kingdom Participation Group, Universidad Nacional Autónoma de México, University of Arizona, University of Colorado Boulder, University of Oxford, University of Portsmouth, University of Utah, University of Virginia, University of Washington, University of Wisconsin, Vanderbilt University, and Yale University.

The CSS survey is funded by the National Aeronautics and Space Administration under Grant No.

NNG05GF22G issued through the Science Mission Directorate Near-Earth Objects Observations Program. The CRTS survey is supported by the U.S. National Science Foundation under grants AST-0909182.

Based on observations obtained with the Samuel Oschin 48-inch Telescope at the Palomar Observatory as part of the Zwicky Transient Facility project. ZTF is supported by the National Science Foundation under Grant No. AST-1440341 and a collaboration including Caltech, IPAC, the Weizmann Institute for Science, the Oskar Klein Center at Stockholm University, the University of Maryland, the University of Washington, Deutsches Elektronen-Synchrotron and Humboldt University, Los Alamos National Laboratories, the TANGO Consortium of Taiwan, the University of Wisconsin at Milwaukee, and Lawrence Berkeley National Laboratories. Operations are conducted by COO, IPAC, and UW.

APPENDIX

A. MEASURING QUASAR PROPERTIES

In this work we employ black hole masses, bolometric luminosities, and K-corrections from [Shen et al. \(2011\)](#) catalog, based on single-epoch SDSS spectra. Here we explain the choices made in the difficult art of estimating each of these quasar physical properties.

It is non-trivial to measure the mass of black holes living in the centers of active galaxies, even provided a detailed spectrum. The most common approach to estimate black hole masses in AGN is to assume that the broad-line region (BLR) is virialized:

$$M_{BH} = f \frac{R \Delta V^2}{G} = f M_{vir} \quad (A1)$$

where f is a constant of order unity, R is the size of the BLR (estimated from emission-line lag Δt as $R = c \Delta t$), ΔV is virial velocity, G gravitational constant ([Shen et al. 2008](#)). From reverberation mapping studies (eg. [Shen et al. 2019](#)) we know that continuum luminosity L is related to the size of the BLR region as $R \propto L^\gamma$ ([Vestergaard & Peterson 2006](#)), with γ very close to 1/2 (eg. [Bentz et al. 2009](#) finds from RM studies $\gamma = 0.519 \pm 0.06$). Thus we find that $R \Delta V^2 \propto L^\gamma \Delta V^2 \equiv \mu$. The virial velocity ΔV is usually estimated from the width of the broad emission lines (or line dispersion). In the absence of a quasar spectrum, there are alternative methods using a conversion of the broad-band photometry into monochromatic fluxes in the vicinity of reverberating lines (eg. [Kozłowski 2015](#), used in [Kozłowski 2017](#) to estimate black hole mass for 280 000 AGN). Depending on the redshift, different rest-frame calibrated emission lines shift into the observed passband: broad H α at 6562Å, H β at 5100Å, Mg II at 2800Å, and C IV at 1350Å (see Fig.7 in [Shen et al. 2019](#), and [Vestergaard 2002](#)). Some authors even consider separately C IV-based and Mg II-based black hole mass estimates. We refer the reader to [Shen et al. \(2008\)](#) who in detail describes various biases and inherent assumptions of virial black hole mass measurements.

Another important quasar property - bolometric luminosity, is most often estimated from the absolute i-band magnitude, M_i (see [Shen et al. 2008](#), Fig.2). M_i is derived from the observed i-band magnitude, by correcting for Galactic extinction, and correcting for the fact that at different redshifts different portions of the spectral energy distribution are observed by the telescope filter bandpass. The latter, known as K-correction $K(z)$ ([Oke & Sandage 1968](#)), is defined as $m_{intrinsic} = m_{observed} - K(z)$. In the early 2000's the common approach was to K-correct to redshift 0, but as ([Richards et al. 2006](#)) pointed out, since the distribution of quasars peaks at redshift 2, for most quasars correcting to the redshift of 0 required shifting the observed spectrum into the far infrared. Moreover, the procedure was to correct separately for the continuum and emission line contributions, assuming a particular spectral shape (eg. power law $f_\nu \propto \nu^\alpha$, with $\alpha = -0.5$ - see [Schneider et al. 2010](#); [Vanden Berk et al. 2001](#); [Richards et al. 2006](#)). This introduces a larger error for K(z=0) than for K(z=2) if the assumed spectral shape $\alpha = -0.5$ is far from the real spectral index.

In early 2010's, after [Richards et al. 2006](#); [Wisotzki 2000](#); [Blanton et al. 2003](#), the practice started shifting towards K-correcting to redshift 2, and including custom quasar spectral shapes, as reflected by the content of [Shen et al. \(2011\)](#) quasar catalog. Thus in this study we use the absolute i-band magnitude K-corrected to $z=2$: $M_i(z=2)$.

These methods were used to create catalogs of quasar properties derived from spectra. Since quasars are variable at ~ 0.2 mag level, the ideal is to use a single-epoch calibrated spectrum to estimate the continuum luminosity, and find virial black hole masses using relationships based on the monochromatic fluxes and broad line widths described above. A glance at the available quasar catalogs reveals that, given any SDSS data release, there is indeed first a catalog of basic quasar properties (redshift and photometry - eg. [Schneider et al. 2007, 2010](#)), and more detailed catalogs containing black hole masses and bolometric luminosities follow (eg. [Shen et al. 2008, 2011](#)). More recently, once SDSS DR12 Quasar Catalog ([Pâris et al. 2017](#)) was released, K17 followed using SDSS photometry as a proxy for monochromatic luminosities. [Chen et al. \(2018\)](#) added a detailed analysis of continuum luminosities in the $H\alpha$, $H\beta$ regions for low-redshift quasars. Using the spectra from Chinese LAMOST survey [Dong et al. \(2018\)](#) also sought to estimate virial black hole masses, and the results, while consistent with [Shen et al. \(2011\)](#), suffered from the necessity to peg the non-calibrated spectra to the SDSS photometry which was taken a different epoch. Thus even though the SDSS DR12 Quasar Catalog of [Pâris et al. \(2018\)](#) is the most recent, like [Pâris et al. \(2017\)](#) it lacks black hole masses and bolometric luminosities, and there is no recent work that re-analyzed the spectral data. Therefore we use black hole mass estimates and monochromatic luminosities from [Shen et al. \(2011\)](#), based directly on single-epoch spectra.

B. CLQSO CANDIDATES

Based on the DRW model parameters τ , σ fitted with *celerite* using the SDSS and PS1 data, we find that there are quasars for which there is a pronounced difference between τ , σ inferred from combined SDSS-PS1 data vs just SDSS. Specifically, Fig. 12 shows that there are objects where $f_\sigma = \log_{10}(\sigma_{\text{SDSS-PS1}}/\sigma_{\text{SDSS}}) > 0.4$ and $f_\tau = \log_{10}(\tau_{\text{SDSS-PS1}}/\tau_{\text{SDSS}}) > 1$ (a tenfold increase in τ and over twofold increase in σ). Visual inspection of objects simultaneously satisfying $f_\sigma > 0.4$ and $f_\tau > 1$ shows that these underwent a significant (> 0.5 mag) change in brightness between the SDSS (baseline 1998 - 2008) and PS1 DR2 observations (2009-2014 - see Fig. 2). Thus DRW fitting could also be a way of finding changing-look quasar (and AGN) candidates. Figs. 22–25 show the SDSS-PS1 r-band light curves of 40 CLQSO candidates, with median PS1 brightness larger than 20.5 mag. The open circles indicate day-averaged epochs (see Sec. 3). Table 5 contains the basic physical parameters for these quasars. Some quasars show a downward trend, like turn-off CLQSO (eg. 123909, 1412379, 1644710), while some are seen in a brightening stage, like turn-on CLQSO (eg. 1976348, 221006, 4069419, 4205621). Quasar 612585 has the largest amount of auxiliary multi-wavelength coverage: x-ray from XMM Newton, UV from Galex, IR from UKIDSS, VHS, WISE, and has been analyzed as part of the x-ray targeted sample of S82 quasars - S82X by [LaMassa et al. \(2016\)](#). Quasar 751557 was previously identified by [MacLeod et al. \(2019\)](#) as a CLQSO candidate, with detailed Magellan spectroscopy described therein. Two quasars: 1003694 and 1299803 have WISE data in the S82X catalog ([LaMassa et al. 2016](#)). Quasars 612585 and 3633437 have X-ray detections in the 3XMM-DR5 catalog ([Rosen et al. 2016](#)), but they have no matches in Chandra point source catalog (second release, [Evans et al. 2010](#); [Evans & Civano 2018](#)). There are no matches against the unified radio catalog of [Kimball & Ivezić \(2008\)](#), which includes FIRST and NVSS data. We especially recommend spectroscopic follow-up of the brightest targets: 1976348 (mean 17.8 mag, turn-on, upper-left panel in Fig. 23), 2104791 (mean 18.4 mag, turn-off, middle-left panel in Fig. 23).

C. MG II VARIABILITY

We searched for dependency of variability parameters on other physical properties, beyond the black hole mass and quasar luminosity employed in Eq. 12. The quasar optical spectrum has certain strong emission lines, depending on the redshift. In particular, the Mg II emission line lags the continuum and is less variable ([Reichert et al. 1994](#)). Mg II line is also an important virial black hole mass estimator for quasars - [McLure & Jarvis \(2002\)](#) noticed that the FWHM of the Mg II doublet trails that of the $H\beta$ line (also see [Shen 2013](#)). Fol-

lowing [Ivezić et al. \(2004\)](#) and [MacLeod et al. \(2012\)](#), we investigated the residuals in data-model(SF_∞) as a function of wavelength. Left hand side panel of Fig. 26 shows the SF_∞ model residuals in the λ_{RF} vs τ_{RF} space. The right hand side panel shows the residuals marginalized along τ_{RF} . The decrement around 2800 Å on the right hand side panel is more pronounced when using combined SDSS-PS1 light curves. We see that both aggregates based on raw data (blue dots) or on medians (black dots) agree - the two statistical methods show a small ($\sim 5\%$), but statistically significant detection of a depression in the 2800 Å region, as expected from theory.

Table 5. CLQSO candidates : catalog information from [Shen et al. \(2011\)](#), concerning DR7 name (dbID) and SDSSJID location (α , δ in degrees, J2000), distance (spectrum-based redshift), physical parameters (bolometric luminosity L_{Bol} erg s $^{-1}$, black hole mass M_{BH}/M_{\odot} , Eddington ratio $f_{Edd} = L_{Bol}/L_{Edd}$), and light curve properties (the difference between median SDSS and PS1 magnitudes $\Delta(\text{mag})$, the difference in scatter between SDSS and PS1 segments $\Delta(\sigma_G)$, and the median PS1 magnitude - see Fig. 14).

dbID	SDSSJID	α	δ	redshift	$\log_{10}(L_{Bol})$	$\log_{10}(M_{BH}/M_{\odot})$	f_{Edd}	$\Delta(\text{mag})$	$\Delta(\sigma_G)$	median PS1
123909	001626.54 + 003632.4	4.111	0.609	3.24	46.57	9.47	-1.0	-0.29	-0.054	20.48
8442	001731.70 + 004910.1	4.382	0.819	2.43	46.61	9.09	-0.58	-0.36	-0.107	20.36
4069419	003359.39 + 000230.0	8.497	0.042	1.64	45.95	9.05	-1.21	0.22	0.017	20.2
221006	005142.20 + 002129.0	12.926	0.358	1.55	45.95	8.24	-0.39	0.21	-0.01	19.97
257776	005513.15 - 005621.2	13.805	-0.939	3.61	47.13	9.58	-0.54	-0.32	-0.242	19.53
612585 ^a	010812.00 - 000516.5	17.05	-0.088	1.0	45.52	9.06	-1.64	-0.37	0.006	20.5
1003694 ^b	012114.19 - 010310.8	20.309	-1.053	1.89	46.59	8.83	-0.34	0.28	0.032	19.11
1299803 ^b	014303.23 - 004354.0	25.763	-0.732	0.53	45.78	8.68	-1.0	-0.18	-0.008	18.56
1644710	021259.00 - 000550.1	33.246	-0.097	0.81	45.67	8.38	-0.81	-0.28	0.022	19.7
1730482	021529.02 - 005314.9	33.871	-0.887	1.37	45.98	8.8	-0.92	0.66	-0.009	19.57
2104791 [*]	022239.83 + 000022.5	35.666	0.006	0.99	46.28	9.33	-1.16	-0.31	0.013	18.66
2061101	022505.06 + 001733.2	36.271	0.293	2.42	46.38	8.09	0.2	-0.34	-0.016	20.15
2006852	023917.86 - 001916.8	39.824	-0.321	1.41	46.07	8.73	-0.76	-0.45	-0.013	20.24
2503955	025316.46 + 010759.7	43.319	1.133	1.03	46.31	8.94	-0.73	-0.39	-0.071	19.07
2484608	025654.42 - 011455.4	44.227	-1.249	0.54	45.57	8.48	-1.01	-0.43	-0.023	19.65
3052176	030504.07 + 011324.5	46.267	1.223	0.61	45.29	9.2	-2.01	-0.35	0.016	20.09
3096136	031401.11 + 011131.6	48.505	1.192	1.31	46.06	9.21	-1.25	-0.27	-0.181	20.09
3147102	031846.13 - 005622.8	49.692	-0.94	2.12	46.57	9.07	-0.6	0.47	-0.078	19.07
3781306	032745.74 + 005217.2	51.941	0.871	1.16	45.77	<i>N/A</i>	<i>N/A</i>	0.19	0.032	19.94
3858587	032825.19 - 003252.3	52.105	-0.548	0.77	45.61	8.68	-1.17	0.33	0.031	19.39
3810874	033047.73 + 004859.4	52.699	0.816	0.86	45.8	8.35	-0.65	-0.1	-0.177	19.8
3739253	033059.05 + 010952.0	52.746	1.164	0.56	45.39	8.16	-0.86	-0.27	0.01	19.72
3791907	033431.17 - 000904.0	53.63	-0.151	1.64	46.01	9.12	-1.21	0.28	0.02	20.29
4913626	034512.62 + 002245.7	56.303	0.379	0.42	45.5	8.81	-1.41	-0.48	-0.055	19.43
4205621	203932.41 - 001818.3	309.885	-0.305	1.58	46.21	8.66	-0.55	0.17	-0.126	19.77
3319354	204952.62 + 011306.6	312.469	1.219	1.09	46.14	9.52	-1.48	-0.91	-0.048	20.08
3633437 ^c	205105.02 - 005847.5	312.771	-0.98	0.54	45.34	8.47	-1.23	-0.51	0.071	20.34
1835106	215015.05 - 005331.4	327.563	-0.892	1.9	46.33	9.21	-0.98	0.69	0.035	19.28
1901056	215055.51 - 001739.4	327.731	-0.294	1.54	46.26	8.6	-0.44	-0.19	0.009	20.46
1976348 [*]	215841.40 - 001507.7	329.673	-0.252	1.46	46.92	9.39	-0.57	0.39	-0.051	17.56
1446022	220535.23 + 000756.3	331.397	0.132	1.69	46.45	9.25	-0.9	0.17	-0.039	19.34
1378415	221347.32 + 001928.4	333.447	0.325	2.31	46.41	8.59	-0.29	0.23	-0.113	20.02
1412379	221831.58 - 004548.9	334.632	-0.764	1.23	46.15	9.48	-1.43	-0.61	-0.057	20.04
1124333	222918.25 - 004003.6	337.326	-0.668	1.16	45.81	8.35	-0.64	-0.28	-0.003	20.12
751557 ^d	225240.37 + 010958.7	343.168	1.166	0.53	45.32	8.88	-1.66	0.39	-0.536	19.67
467617	231032.17 - 011449.5	347.634	-1.247	1.82	46.03	7.86	0.06	0.23	0.024	20.18
568312	231953.07 - 010139.0	349.971	-1.028	1.15	45.6	8.29	-0.79	0.33	0.005	19.79
292959	232030.97 - 004039.2	350.129	-0.678	1.72	46.69	9.39	-0.8	-0.22	-0.009	19.07
3976336	235213.27 - 004326.3	358.055	-0.724	0.9	45.64	8.85	-1.3	-0.18	-0.08	19.92
3946479	235248.71 - 001518.4	358.203	-0.255	1.34	45.8	9.01	-1.3	-0.07	-0.025	20.26

^{*}Recommended for follow-up

^aS82X ([LaMassa et al. 2016](#)), XMM Newton, Galex UV, UKIDSS, VHS, WISE

^bS82X ([LaMassa et al. 2019](#)), WISE

^cIn 3XMM-DR5 x-ray catalog ([Rosen et al. 2016](#))

^dM19, CLQSO candidate, Magellan follow-up

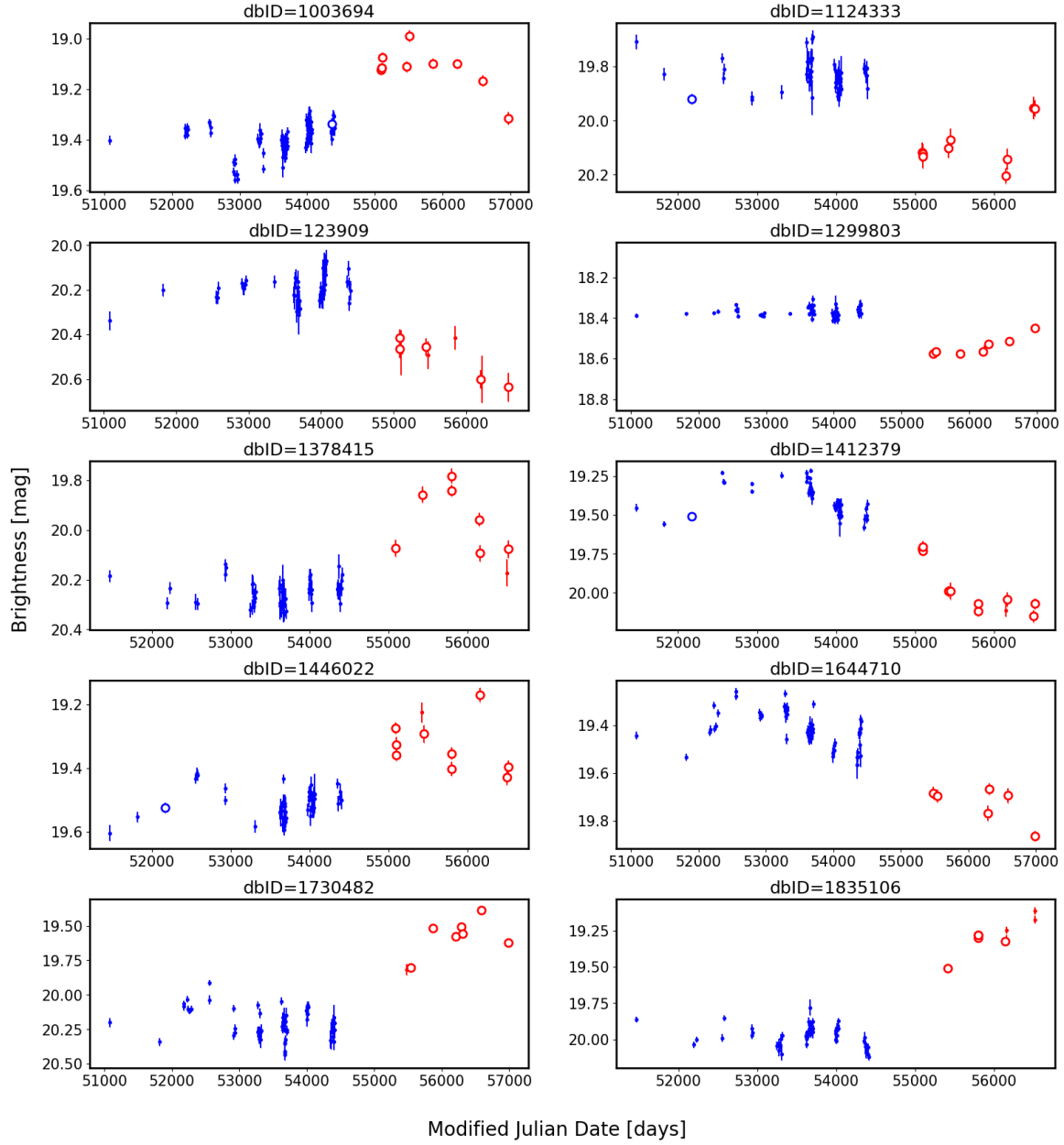


Figure 22. Outliers in the space of recovered DRW parameters between SDSS and SDSS-PS1, as well as median offsets. Page 1.

REFERENCES

- AlSayyad, Y. 2016, PhD thesis, University of Washington.
<http://hdl.handle.net/1773/37020>
- Annis, J., Soares-Santos, M., Strauss, M. A., et al. 2014, *ApJ*, 794, 120, doi: [10.1088/0004-637X/794/2/120](https://doi.org/10.1088/0004-637X/794/2/120)
- Aranzana, E., K rding, E., Uttley, P., Scaringi, S., & Bloemen, S. 2018, *MNRAS*, 476, 2501, doi: [10.1093/mnras/sty413](https://doi.org/10.1093/mnras/sty413)
- Babi c, A., Miller, L., Jarvis, M. J., et al. 2007, *A&A*, 474, 755, doi: [10.1051/0004-6361:20078286](https://doi.org/10.1051/0004-6361:20078286)
- Balbus, S. A. 2003, *ARA&A*, 41, 555, doi: [10.1146/annurev.astro.41.081401.155207](https://doi.org/10.1146/annurev.astro.41.081401.155207)
- Balbus, S. A., & Hawley, J. F. 1998, *Reviews of Modern Physics*, 70, 1, doi: [10.1103/RevModPhys.70.1](https://doi.org/10.1103/RevModPhys.70.1)
- Bauer, A., Baltay, C., Coppi, P., et al. 2009, *ApJ*, 696, 1241, doi: [10.1088/0004-637X/696/2/1241](https://doi.org/10.1088/0004-637X/696/2/1241)
- Bellm, E. C., Kulkarni, S. R., Graham, M. J., et al. 2019, *PASP*, 131, 018002, doi: [10.1088/1538-3873/aaecbe](https://doi.org/10.1088/1538-3873/aaecbe)

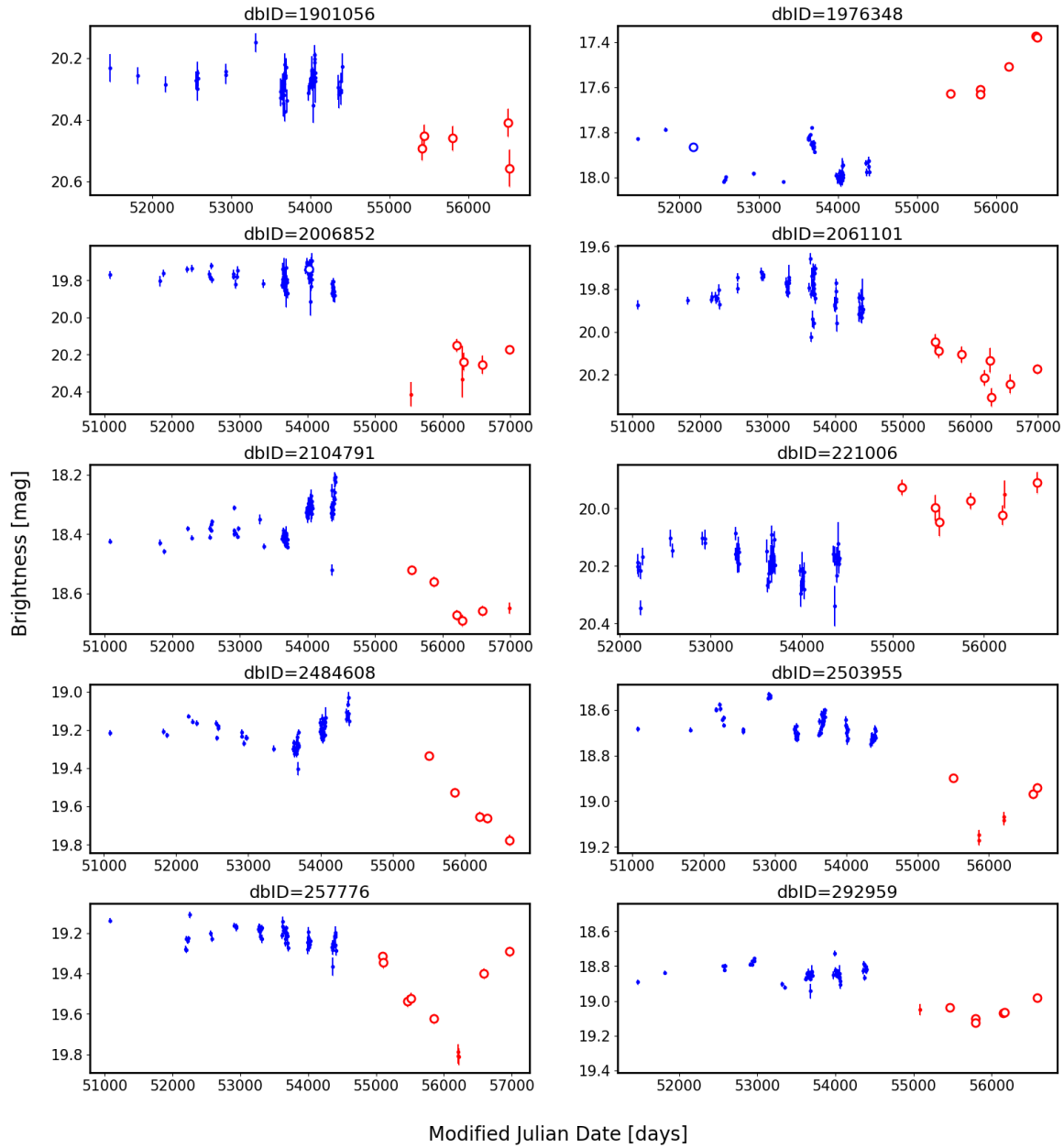


Figure 23. As Fig. 22, page 2.

Bentz, M. C., Peterson, B. M., Netzer, H., Pogge, R. W., & Vestergaard, M. 2009, *ApJ*, 697, 160, doi: [10.1088/0004-637X/697/1/160](https://doi.org/10.1088/0004-637X/697/1/160)

Bianchi, S., Piconcelli, E., Chiaberge, M., et al. 2009, *ApJ*, 695, 781, doi: [10.1088/0004-637X/695/1/781](https://doi.org/10.1088/0004-637X/695/1/781)

Blanchard, P. K., Nicholl, M., Berger, E., et al. 2017, *The Astrophysical Journal*, 843, 106, doi: [10.3847/1538-4357/aa77f7](https://doi.org/10.3847/1538-4357/aa77f7)

Blanton, M. R., Lin, H., Lupton, R. H., et al. 2003, *AJ*, 125, 2276, doi: [10.1086/344761](https://doi.org/10.1086/344761)

Borucki, W. J., Koch, D., Basri, G., et al. 2010, *Science*, 327, 977, doi: [10.1126/science.1185402](https://doi.org/10.1126/science.1185402)

Cackett, E. M., Gültekin, K., Bentz, M. C., et al. 2015, *ApJ*, 810, 86, doi: [10.1088/0004-637X/810/2/86](https://doi.org/10.1088/0004-637X/810/2/86)

Cai, Z.-Y., Wang, J.-X., Gu, W.-M., et al. 2016, *ApJ*, 826, 7, doi: [10.3847/0004-637X/826/1/7](https://doi.org/10.3847/0004-637X/826/1/7)

Cai, Z.-Y., Wang, J.-X., Zhu, F.-F., et al. 2018, *The Astrophysical Journal*, 855, 117, doi: [10.3847/1538-4357/aab091](https://doi.org/10.3847/1538-4357/aab091)

Caplar, N., Lilly, S. J., & Trakhtenbrot, B. 2017, *ApJ*, 834, 111, doi: [10.3847/1538-4357/834/2/111](https://doi.org/10.3847/1538-4357/834/2/111)

Chambers, K. C., Magnier, E. A., Metcalfe, N., et al. 2016, *arXiv e-prints*, arXiv:1612.05560, <https://arxiv.org/abs/1612.05560>

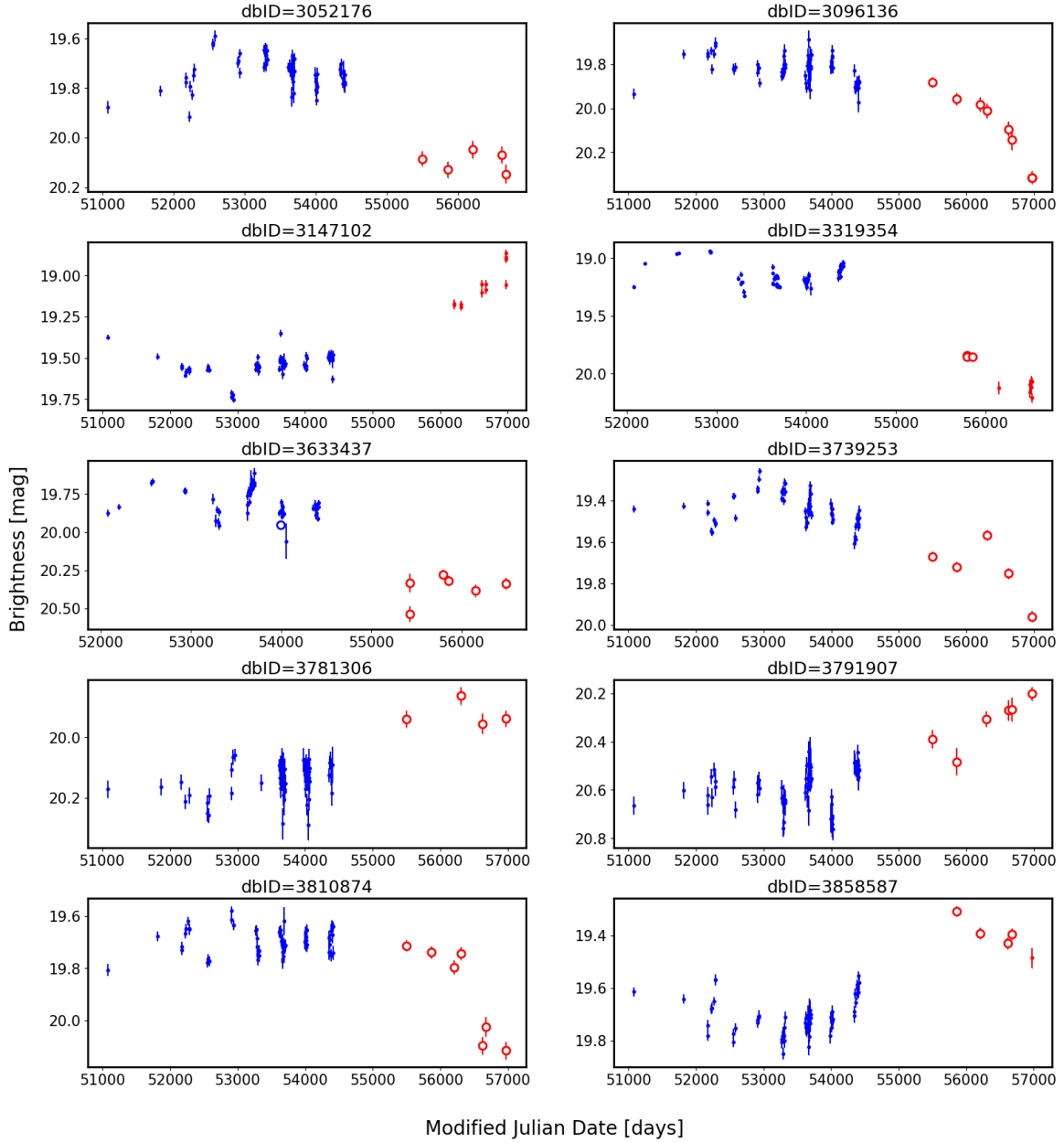


Figure 24. As Fig. 22, page 3.

Charisi, M., Bartos, I., Haiman, Z., et al. 2016, MNRAS, 463, 2145, doi: [10.1093/mnras/stw1838](https://doi.org/10.1093/mnras/stw1838)

Chen, Z.-F., Pan, D.-S., Pang, T.-T., & Huang, Y. 2018, ApJS, 234, 16, doi: [10.3847/1538-4365/aa9d90](https://doi.org/10.3847/1538-4365/aa9d90)

Curran, S. J., & Moss, J. P. 2019, A&A, 629, A56, doi: [10.1051/0004-6361/201936179](https://doi.org/10.1051/0004-6361/201936179)

Czerny, B. 2006, in Astronomical Society of the Pacific Conference Series, Vol. 360, AGN Variability from X-Rays to Radio Waves, ed. C. M. Gaskell, I. M. McHardy, B. M. Peterson, & S. G. Sergeev, 265

Dexter, J., & Agol, E. 2011, ApJL, 727, L24, doi: [10.1088/2041-8205/727/1/L24](https://doi.org/10.1088/2041-8205/727/1/L24)

Dexter, J., & Begelman, M. C. 2019, MNRAS, 483, L17, doi: [10.1093/mnrasl/sly213](https://doi.org/10.1093/mnrasl/sly213)

Dong, X. Y., Wu, X.-B., Ai, Y. L., et al. 2018, AJ, 155, 189, doi: [10.3847/1538-3881/aab5ae](https://doi.org/10.3847/1538-3881/aab5ae)

Drake, A. J., Djorgovski, S. G., Mahabal, A., et al. 2009, ApJ, 696, 870, doi: [10.1088/0004-637X/696/1/870](https://doi.org/10.1088/0004-637X/696/1/870)

Eardley, D. M., & Lightman, A. P. 1975, ApJ, 200, 187, doi: [10.1086/153777](https://doi.org/10.1086/153777)

Edelson, R., Vaughan, S., Malkan, M., et al. 2014, ApJ, 795, 2, doi: [10.1088/0004-637X/795/1/2](https://doi.org/10.1088/0004-637X/795/1/2)

Edelson, R., Gelbord, J. M., Horne, K., et al. 2015, ApJ, 806, 129, doi: [10.1088/0004-637X/806/1/129](https://doi.org/10.1088/0004-637X/806/1/129)

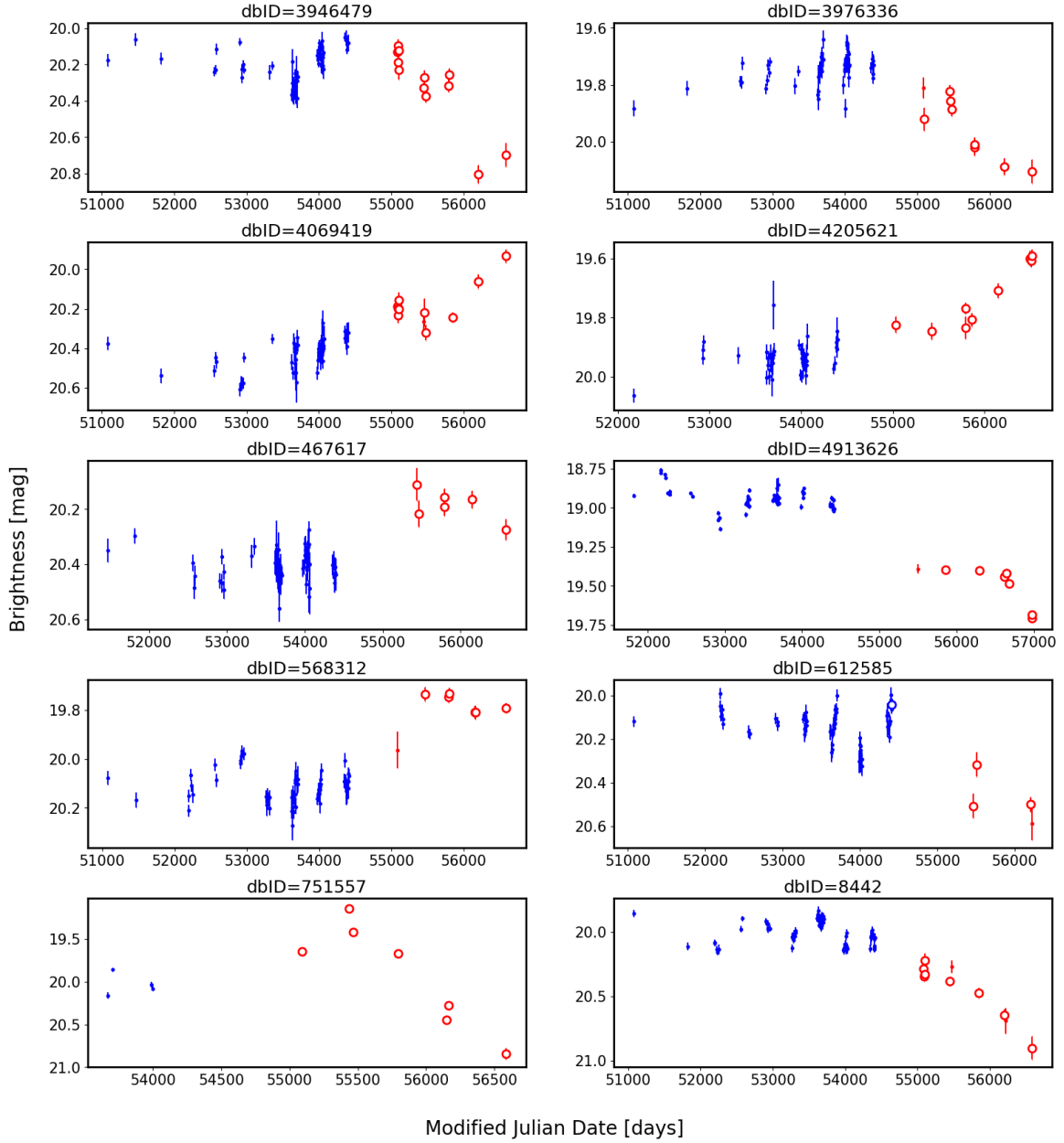


Figure 25. As Fig. 22, page 4.

Elitzur, M., Ho, L. C., & Trump, J. R. 2014, MNRAS, 438, 3340, doi: [10.1093/mnras/stt2445](https://doi.org/10.1093/mnras/stt2445)

Evans, I. N., & Civano, F. 2018, Astronomy and Geophysics, 59, 2.17, doi: [10.1093/astrogeo/aty079](https://doi.org/10.1093/astrogeo/aty079)

Evans, I. N., Primini, F. A., Glotfelty, K. J., et al. 2010, The Astrophysical Journal Supplement Series, 189, 37, doi: [10.1088/0067-0049/189/1/37](https://doi.org/10.1088/0067-0049/189/1/37)

Fausnaugh, M. M., Denney, K. D., Barth, A. J., et al. 2016, ApJ, 821, 56, doi: [10.3847/0004-637X/821/1/56](https://doi.org/10.3847/0004-637X/821/1/56)

Fausnaugh, M. M., Starkey, D. A., Horne, K., et al. 2018, ApJ, 854, 107, doi: [10.3847/1538-4357/aaa2b](https://doi.org/10.3847/1538-4357/aaa2b)

Ferrarese, L., & Merritt, D. 2000, The Astrophysical Journal, 539, L9, doi: [10.1086/312838](https://doi.org/10.1086/312838)

Flewelling, H. 2018, in American Astronomical Society Meeting Abstracts, Vol. 231, American Astronomical Society Meeting Abstracts 231, 436.01

Flewelling, H. A., Magnier, E. A., Chambers, K. C., et al. 2016, arXiv e-prints, arXiv:1612.05243. <https://arxiv.org/abs/1612.05243>

Foreman-Mackey, D., Agol, E., Ambikasaran, S., & Angus, R. 2017, AJ, 154, 220, doi: [10.3847/1538-3881/aa9332](https://doi.org/10.3847/1538-3881/aa9332)

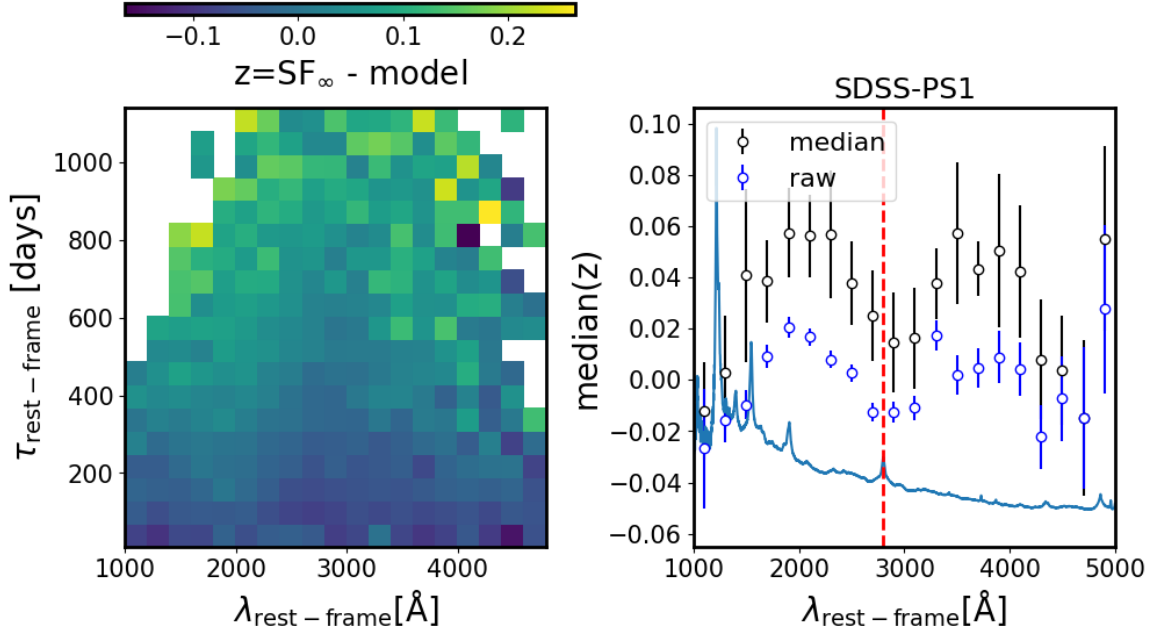


Figure 26. The data-model residuals after fitting Eq. 12 to the quasar SF_{∞} , using SDSS-PS1 quasar light curves. The left panel shows the residuals as a function of λ_{RF} and τ_{RF} . The right panel shows the median of residuals marginalized along τ_{RF} , with error on the median based on the scatter in λ_{RF} bins : $\sigma_{\text{median}} = 1.25\text{RMS}_{\text{bin}}/\sqrt{N_{\text{bin}}}$, where RMS_{bin} is estimated from the robust Gaussian interquartile-based σ_G (Ivezić et al. 2014). Black circles are medians based on the averages plotted on the left (N_{bin} is between 7 and 20, depending on the number of non-empty bins on the left hand side panel), and blue dots are medians based on the raw data (N_{bin} varies as a function of λ_{RF} , from a few to 800, peaking at about 2500 Å, reflecting the fact that the quasar distribution peaks at redshift $z = 2$). We overplot the composite quasar spectrum from Vanden Berk et al. (2001), and mark with vertical dashed red line the location of the Mg II 2798 Å line.

Frank, J., King, A., & Raine, D. J. 2002, *Accretion Power in Astrophysics: Third Edition* (Cambridge University Press), 398

Frederick, S., Gezari, S., Graham, M. J., et al. 2019, arXiv e-prints, arXiv:1904.10973.
<https://arxiv.org/abs/1904.10973>

Gardner, E., & Done, C. 2017, *Monthly Notices of the Royal Astronomical Society*, 470, 3591,
doi: [10.1093/mnras/stx946](https://doi.org/10.1093/mnras/stx946)

Gezari, S., Hung, T., Cenko, S. B., et al. 2017, *The Astrophysical Journal*, 835, 144,
doi: [10.3847/1538-4357/835/2/144](https://doi.org/10.3847/1538-4357/835/2/144)

Graham, M. J., Djorgovski, S. G., Stern, D., et al. 2015, *Nature*, 518, 74, doi: [10.1038/nature14143](https://doi.org/10.1038/nature14143)

Graham, M. J., Ross, N. P., Stern, D., et al. 2019, arXiv e-prints, arXiv:1905.02262.
<https://arxiv.org/abs/1905.02262>

Grzędzielski, M., Janiuk, A., Czerny, B., & Wu, Q. 2017, *A&A*, 603, A110, doi: [10.1051/0004-6361/201629672](https://doi.org/10.1051/0004-6361/201629672)

Guo, H., Wang, J., Cai, Z., & Sun, M. 2017, *ApJ*, 847, 132,
doi: [10.3847/1538-4357/aa8d71](https://doi.org/10.3847/1538-4357/aa8d71)

Guo, H., Malkan, M. A., Gu, M., et al. 2016, *The Astrophysical Journal*, 826, 186,
doi: [10.3847/0004-637x/826/2/186](https://doi.org/10.3847/0004-637x/826/2/186)

Guo, H., Shen, Y., He, Z., et al. 2019, arXiv e-prints.
<https://arxiv.org/abs/1907.06669>

Hameury, J.-M., Viallet, M., & Lasota, J.-P. 2009, *A&A*, 496, 413, doi: [10.1051/0004-6361/200810928](https://doi.org/10.1051/0004-6361/200810928)

Hawkins, M. R. S. 2007, *Astronomy and Astrophysics*, 462, 581, doi: [10.1051/0004-6361:20066283](https://doi.org/10.1051/0004-6361:20066283)

Hernitschek, N., Schlafly, E. F., Sesar, B., et al. 2016, *The Astrophysical Journal*, 817, 73

Hopkins, P. F., Hernquist, L., Martini, P., et al. 2005, *ApJL*, 625, L71, doi: [10.1086/431146](https://doi.org/10.1086/431146)

Ivezić, Ž., Connolly, A. J., VanderPlas, J. T., & Gray, A. 2014, *Statistics, Data Mining, and Machine Learning in Astronomy*

Ivezić, Ž., Lupton, R. H., Juric, M., et al. 2004, in *IAU Symposium, Vol. 222, The Interplay Among Black Holes, Stars and ISM in Galactic Nuclei*, ed. T. Storchi-Bergmann, L. C. Ho, & H. R. Schmitt, 525–526

Ivezić, Ž., Smith, J. A., Miknaitis, G., et al. 2007, *AJ*, 134, 973, doi: [10.1086/519976](https://doi.org/10.1086/519976)

Ivezić, Ž., Kahn, S. M., Tyson, J. A., et al. 2019, *ApJ*, 873, 111, doi: [10.3847/1538-4357/ab042c](https://doi.org/10.3847/1538-4357/ab042c)

Jiang, Y.-F., Davis, S. W., & Stone, J. M. 2016, *ApJ*, 827, 10, doi: [10.3847/0004-637X/827/1/10](https://doi.org/10.3847/0004-637X/827/1/10)

- Jin, X., Zhang, Y., Zhang, J., et al. 2019, *MNRAS*, 485, 4539, doi: [10.1093/mnras/stz680](https://doi.org/10.1093/mnras/stz680)
- Kasliwal, V. P., Vogeley, M. S., & Richards, G. T. 2015, *MNRAS*, 451, 4328, doi: [10.1093/mnras/stv1230](https://doi.org/10.1093/mnras/stv1230)
- Kelly, B. C. 2007, *ApJ*, 665, 1489, doi: [10.1086/519947](https://doi.org/10.1086/519947)
- Kelly, B. C., Bechtold, J., & Siemiginowska, A. 2009, *The Astrophysical Journal*, 698, 895
- Kelly, B. C., Becker, A. C., Sobolewska, M., Siemiginowska, A., & Uttley, P. 2014, *ApJ*, 788, 33, doi: [10.1088/0004-637X/788/1/33](https://doi.org/10.1088/0004-637X/788/1/33)
- Kelly, B. C., Treu, T., Malkan, M., Pancoast, A., & Woo, J.-H. 2013, *ApJ*, 779, 187, doi: [10.1088/0004-637X/779/2/187](https://doi.org/10.1088/0004-637X/779/2/187)
- Kimball, A. E., & Ivezić, Ž. 2008, *The Astronomical Journal*, 136, 684, doi: [10.1088/0004-6256/136/2/684](https://doi.org/10.1088/0004-6256/136/2/684)
- Kokubo, M. 2015, *MNRAS*, 449, 94, doi: [10.1093/mnras/stv241](https://doi.org/10.1093/mnras/stv241)
- Kollmeier, J. A., Zasowski, G., Rix, H.-W., et al. 2017, arXiv e-prints, arXiv:1711.03234, <https://arxiv.org/abs/1711.03234>
- Kormendy, J., & Ho, L. C. 2013, *ARA&A*, 51, 511, doi: [10.1146/annurev-astro-082708-101811](https://doi.org/10.1146/annurev-astro-082708-101811)
- Kozłowski, S. 2015, *AcA*, 65, 251, <https://arxiv.org/abs/1504.05960>
- Kozłowski, S. 2016, *MNRAS*, 459, 2787, doi: [10.1093/mnras/stw819](https://doi.org/10.1093/mnras/stw819)
- Kozłowski, S. 2017, *ApJS*, 228, 9, doi: [10.3847/1538-4365/228/1/9](https://doi.org/10.3847/1538-4365/228/1/9)
- Kozłowski, S., Kochanek, C. S., Ashby, M. L. N., et al. 2016, *ApJ*, 817, 119, doi: [10.3847/0004-637X/817/2/119](https://doi.org/10.3847/0004-637X/817/2/119)
- Kozłowski, S., Kochanek, C. S., Udalski, A., et al. 2010, *ApJ*, 708, 927
- Kozłowski, Szymon. 2017, *A&A*, 597, A128, doi: [10.1051/0004-6361/201629890](https://doi.org/10.1051/0004-6361/201629890)
- Krolik, J. H., Horne, K., Kallman, T. R., et al. 1991, *ApJ*, 371, 541, doi: [10.1086/169918](https://doi.org/10.1086/169918)
- Kubota, A., & Done, C. 2018, *MNRAS*, 480, 1247, doi: [10.1093/mnras/sty1890](https://doi.org/10.1093/mnras/sty1890)
- Labita, M., Decarli, R., Treves, A., & Falomo, R. 2009, *MNRAS*, 399, 2099, doi: [10.1111/j.1365-2966.2009.15400.x](https://doi.org/10.1111/j.1365-2966.2009.15400.x)
- LaMassa, S. M., Georgakakis, A., Vivek, M., et al. 2019, *ApJ*, 876, 50, doi: [10.3847/1538-4357/ab108b](https://doi.org/10.3847/1538-4357/ab108b)
- LaMassa, S. M., Cales, S., Moran, E. C., et al. 2015, *ApJ*, 800, 144, doi: [10.1088/0004-637X/800/2/144](https://doi.org/10.1088/0004-637X/800/2/144)
- LaMassa, S. M., Urry, C. M., Cappelluti, N., et al. 2016, *ApJ*, 817, 172, doi: [10.3847/0004-637X/817/2/172](https://doi.org/10.3847/0004-637X/817/2/172)
- Lasota, J.-P. 2016, in *Astrophysics and Space Science Library*, Vol. 440, *Astrophysics of Black Holes: From Fundamental Aspects to Latest Developments*, ed. C. Bambi, 1
- Lawrence, A. 2018, *Nature Astronomy*, 2, 102, doi: [10.1038/s41550-017-0372-1](https://doi.org/10.1038/s41550-017-0372-1)
- Li, S.-L., & Cao, X. 2008, *MNRAS*, 387, L41, doi: [10.1111/j.1745-3933.2008.00480.x](https://doi.org/10.1111/j.1745-3933.2008.00480.x)
- Li, Z., McGreer, I. D., Wu, X.-B., Fan, X., & Yang, Q. 2018, *ApJ*, 861, 6, doi: [10.3847/1538-4357/aac6ce](https://doi.org/10.3847/1538-4357/aac6ce)
- Lira, P., Arévalo, P., Uttley, P., McHardy, I. M. M., & Videla, L. 2015, *MNRAS*, 454, 368, doi: [10.1093/mnras/stv1945](https://doi.org/10.1093/mnras/stv1945)
- MacLeod, C. L., Ivezić, Ž., Kochanek, C. S., et al. 2010, *The Astrophysical Journal*, 721, 1014
- MacLeod, C. L., Brooks, K., Ivezić, Ž., et al. 2011, *The Astrophysical Journal*, 728, 26
- MacLeod, C. L., Ivezić, Ž., Sesar, B., et al. 2012, *The Astrophysical Journal*, 753, 106
- MacLeod, C. L., Ross, N. P., Lawrence, A., et al. 2016, *MNRAS*, 457, 389, doi: [10.1093/mnras/stv2997](https://doi.org/10.1093/mnras/stv2997)
- MacLeod, C. L., Green, P. J., Anderson, S. F., et al. 2019, *ApJ*, 874, 8, doi: [10.3847/1538-4357/ab05e2](https://doi.org/10.3847/1538-4357/ab05e2)
- Marchese, E., Braitto, V., Della Ceca, R., Caccianiga, A., & Severgnini, P. 2012, *Monthly Notices of the Royal Astronomical Society*, 421, 1803, doi: [10.1111/j.1365-2966.2012.20445.x](https://doi.org/10.1111/j.1365-2966.2012.20445.x)
- Martini, P., & Schneider, D. P. 2003, *ApJL*, 597, L109, doi: [10.1086/379888](https://doi.org/10.1086/379888)
- Marziani, P., Dultzin, D., Sulentic, J. W., et al. 2018, *Frontiers in Astronomy and Space Sciences*, 5, 6, doi: [10.3389/fspas.2018.00006](https://doi.org/10.3389/fspas.2018.00006)
- Masci, F. J., Laher, R. R., Rusholme, B., et al. 2019, *PASP*, 131, 018003, doi: [10.1088/1538-3873/aae8ac](https://doi.org/10.1088/1538-3873/aae8ac)
- McGreer, I. D., Fan, X., Jiang, L., & Cai, Z. 2018, *AJ*, 155, 131, doi: [10.3847/1538-3881/aaaab4](https://doi.org/10.3847/1538-3881/aaaab4)
- McGreer, I. D., Jiang, L., Fan, X., et al. 2013, *ApJ*, 768, 105, doi: [10.1088/0004-637X/768/2/105](https://doi.org/10.1088/0004-637X/768/2/105)
- McHardy, I. M., Connolly, S. D., Horne, K., et al. 2018, *MNRAS*, 480, 2881, doi: [10.1093/mnras/sty1983](https://doi.org/10.1093/mnras/sty1983)
- McLure, R. J., & Dunlop, J. S. 2004, *MNRAS*, 352, 1390, doi: [10.1111/j.1365-2966.2004.08034.x](https://doi.org/10.1111/j.1365-2966.2004.08034.x)
- McLure, R. J., & Jarvis, M. J. 2002, *MNRAS*, 337, 109, doi: [10.1046/j.1365-8711.2002.05871.x](https://doi.org/10.1046/j.1365-8711.2002.05871.x)
- Morganson, E., Burgett, W. S., Chambers, K. C., et al. 2014, *ApJ*, 784, 92, doi: [10.1088/0004-637X/784/2/92](https://doi.org/10.1088/0004-637X/784/2/92)
- Mushotzky, R. F., Edelson, R., Baumgartner, W., & Gandhi, P. 2011, *The Astrophysical Journal*, 743, L12, doi: [10.1088/2041-8205/743/1/112](https://doi.org/10.1088/2041-8205/743/1/112)

- Netzer, H. 2013, *The Physics and Evolution of Active Galactic Nuclei* (Cambridge University Press)
- Noda, H., & Done, C. 2018, *MNRAS*, 480, 3898, doi: [10.1093/mnras/sty2032](https://doi.org/10.1093/mnras/sty2032)
- Oke, J. B., & Sandage, A. 1968, *ApJ*, 154, 21, doi: [10.1086/149737](https://doi.org/10.1086/149737)
- Palanque-Delabrouille, N., Magneville, C., Yèche, C., et al. 2013, *A&A*, 551, A29, doi: [10.1051/0004-6361/201220379](https://doi.org/10.1051/0004-6361/201220379)
- Panda, S., Czerny, B., Done, C., & Kubota, A. 2019a, *ApJ*, 875, 133, doi: [10.3847/1538-4357/ab11cb](https://doi.org/10.3847/1538-4357/ab11cb)
- Panda, S., Marziani, P., & Czerny, B. 2019b, arXiv e-prints, arXiv:1905.01729. <https://arxiv.org/abs/1905.01729>
- Pâris, I., Petitjean, P., Ross, N. P., et al. 2017, *A&A*, 597, A79, doi: [10.1051/0004-6361/201527999](https://doi.org/10.1051/0004-6361/201527999)
- Pâris, I., Petitjean, P., Aubourg, É., et al. 2018, *A&A*, 613, A51, doi: [10.1051/0004-6361/201732445](https://doi.org/10.1051/0004-6361/201732445)
- Rakshit, S., & Stalin, C. S. 2017, *ApJ*, 842, 96, doi: [10.3847/1538-4357/aa72fa](https://doi.org/10.3847/1538-4357/aa72fa)
- Rasmussen, C. E., & Williams, C. K. I. 2006, *Gaussian Processes for Machine Learning* (Cambridge, MA: MIT Press)
- Rau, A., Kulkarni, S. R., Law, N. M., et al. 2009, *PASP*, 121, 1334, doi: [10.1086/605911](https://doi.org/10.1086/605911)
- Reichert, G. A., Rodriguez-Pascual, P. M., Alloin, D., et al. 1994, *ApJ*, 425, 582, doi: [10.1086/174007](https://doi.org/10.1086/174007)
- Richards, G. T., Strauss, M. A., Fan, X., et al. 2006, *AJ*, 131, 2766, doi: [10.1086/503559](https://doi.org/10.1086/503559)
- Richards, G. T., Myers, A. D., Peters, C. M., et al. 2015, *ApJS*, 219, 39, doi: [10.1088/0067-0049/219/2/39](https://doi.org/10.1088/0067-0049/219/2/39)
- Ricker, G. R., Winn, J. N., Vanderspek, R., et al. 2014, in *Proc. SPIE*, Vol. 9143, *Space Telescopes and Instrumentation 2014: Optical, Infrared, and Millimeter Wave*, 914320
- Riess, A. G., Casertano, S., Yuan, W., Macri, L. M., & Scolnic, D. 2019, *ApJ*, 876, 85, doi: [10.3847/1538-4357/ab1422](https://doi.org/10.3847/1538-4357/ab1422)
- Risaliti, G., Miniutti, G., Elvis, M., et al. 2009, *The Astrophysical Journal*, 696, 160, doi: [10.1088/0004-637x/696/1/160](https://doi.org/10.1088/0004-637x/696/1/160)
- Rosen, S. R., Webb, N. A., Watson, M. G., et al. 2016, *A&A*, 590, A1, doi: [10.1051/0004-6361/201526416](https://doi.org/10.1051/0004-6361/201526416)
- Ross, N. P., McGreer, I. D., White, M., et al. 2013, *ApJ*, 773, doi: [10.1088/0004-637X/773/1/14](https://doi.org/10.1088/0004-637X/773/1/14)
- Ross, N. P., Ford, K. E. S., Graham, M., et al. 2018, *MNRAS*, 480, 4468, doi: [10.1093/mnras/sty2002](https://doi.org/10.1093/mnras/sty2002)
- Ruan, J. J., Anderson, S. F., Dexter, J., & Agol, E. 2014, *The Astrophysical Journal*, 783, 105, doi: [10.1088/0004-637x/783/2/105](https://doi.org/10.1088/0004-637x/783/2/105)
- Ruan, J. J., Anderson, S. F., Eracleous, M., et al. 2019, arXiv e-prints, arXiv:1903.02553. <https://arxiv.org/abs/1903.02553>
- Ruan, J. J., Anderson, S. F., Cales, S. L., et al. 2016, *ApJ*, 826, 188, doi: [10.3847/0004-637X/826/2/188](https://doi.org/10.3847/0004-637X/826/2/188)
- Rumbaugh, N., Shen, Y., Morganson, E., et al. 2018, *ApJ*, 854, 160, doi: [10.3847/1538-4357/aaa9b6](https://doi.org/10.3847/1538-4357/aaa9b6)
- Runnoe, J. C., Cales, S., Ruan, J. J., et al. 2016, *MNRAS*, 455, 1691, doi: [10.1093/mnras/stv2385](https://doi.org/10.1093/mnras/stv2385)
- Rybicki, G. B., & Press, W. H. 1992, *ApJ*, 398, 169, doi: [10.1086/171845](https://doi.org/10.1086/171845)
- Sánchez-Sáez, P., Lira, P., Mejía-Restrepo, J., et al. 2018, *ApJ*, 864, 87, doi: [10.3847/1538-4357/aad7f9](https://doi.org/10.3847/1538-4357/aad7f9)
- Scaringi, S., Maccarone, T. J., Kording, E., et al. 2015, *Science Advances*, 1, e1500686, doi: [10.1126/sciadv.1500686](https://doi.org/10.1126/sciadv.1500686)
- Schawinski, K., Koss, M., Berney, S., & Sartori, L. F. 2015, *Monthly Notices of the Royal Astronomical Society*, 451, 2517, doi: [10.1093/mnras/stv1136](https://doi.org/10.1093/mnras/stv1136)
- Schmidt, K. B., Marshall, P. J., Rix, H.-W., et al. 2010, *ApJ*, 714, 1194, doi: [10.1088/0004-637X/714/2/1194](https://doi.org/10.1088/0004-637X/714/2/1194)
- Schneider, D. P., Hall, P. B., Richards, G. T., et al. 2007, *AJ*, 134, 102, doi: [10.1086/518474](https://doi.org/10.1086/518474)
- . 2008, *VizieR Online Data Catalog*, 7252
- Schneider, D. P., Richards, G. T., Hall, P. B., et al. 2010, *AJ*, 139, 2360, doi: [10.1088/0004-6256/139/6/2360](https://doi.org/10.1088/0004-6256/139/6/2360)
- Sesar, B., Ivezić, Ž., Lupton, R. H., et al. 2007, *AJ*, 134, 2236
- Shakura, N. I., & Sunyaev, R. A. 1973, *A&A*, 24, 337
- Shen, Y. 2013, *Bulletin of the Astronomical Society of India*, 41, 61. <https://arxiv.org/abs/1302.2643>
- Shen, Y., Greene, J. E., Strauss, M. A., Richards, G. T., & Schneider, D. P. 2008, *ApJ*, 680, 169, doi: [10.1086/587475](https://doi.org/10.1086/587475)
- Shen, Y., & Ho, L. C. 2014, *Nature*, 513, 210, doi: [10.1038/nature13712](https://doi.org/10.1038/nature13712)
- Shen, Y., Richards, G. T., Strauss, M. A., et al. 2011, *ApJS*, 194, 45, doi: [10.1088/0067-0049/194/2/45](https://doi.org/10.1088/0067-0049/194/2/45)
- Shen, Y., Hall, P. B., Horne, K., et al. 2019, *ApJS*, 241, 34, doi: [10.3847/1538-4365/ab074f](https://doi.org/10.3847/1538-4365/ab074f)
- Sheng, Z., Wang, T., Jiang, N., et al. 2017, *The Astrophysical Journal*, 846, L7, doi: [10.3847/2041-8213/aa85de](https://doi.org/10.3847/2041-8213/aa85de)
- Sheng, Z., Wang, T., Jiang, N., et al. 2019, arXiv e-prints, arXiv:1905.02904. <https://arxiv.org/abs/1905.02904>
- Simm, T., Salvato, M., Saglia, R., et al. 2016, *A&A*, 585, A129, doi: [10.1051/0004-6361/201527353](https://doi.org/10.1051/0004-6361/201527353)
- Smith, K. L., Mushotzky, R. F., Boyd, P. T., et al. 2018, *ApJ*, 857, 141, doi: [10.3847/1538-4357/aab88d](https://doi.org/10.3847/1538-4357/aab88d)
- Śniegowska, M., & Czerny, B. 2019, arXiv e-prints, arXiv:1904.06767. <https://arxiv.org/abs/1904.06767>

- Stern, D., Graham, M. J., Arav, N., et al. 2017, *ApJ*, 839, 106, doi: [10.3847/1538-4357/aa683c](https://doi.org/10.3847/1538-4357/aa683c)
- Stern, D., McKernan, B., Graham, M. J., et al. 2018, *ApJ*, 864, 27, doi: [10.3847/1538-4357/aac726](https://doi.org/10.3847/1538-4357/aac726)
- Suberlak, K., Ivezić, Ž., MacLeod, C. L., Graham, M., & Sesar, B. 2017, *MNRAS*, 472, 4870, doi: [10.1093/mnras/stx2310](https://doi.org/10.1093/mnras/stx2310)
- Sun, J., & Shen, Y. 2015, *ApJL*, 804, L15, doi: [10.1088/2041-8205/804/1/L15](https://doi.org/10.1088/2041-8205/804/1/L15)
- Sun, M., Xue, Y., Wang, J., Cai, Z., & Guo, H. 2018, *ApJ*, 866, 74, doi: [10.3847/1538-4357/aae208](https://doi.org/10.3847/1538-4357/aae208)
- Trakhtenbrot, B., Arcavi, I., Ricci, C., et al. 2019, *Nature Astronomy*, 3, 242, doi: [10.1038/s41550-018-0661-3](https://doi.org/10.1038/s41550-018-0661-3)
- Vanden Berk, D. E., Richards, G. T., Bauer, A., et al. 2001, *AJ*, 122, 549, doi: [10.1086/321167](https://doi.org/10.1086/321167)
- Vanden Berk, D. E., Wilhite, B. C., Kron, R. G., et al. 2004, *ApJ*, 601, 692, doi: [10.1086/380563](https://doi.org/10.1086/380563)
- Vestergaard, M. 2002, *ApJ*, 571, 733, doi: [10.1086/340045](https://doi.org/10.1086/340045)
- Vestergaard, M., & Peterson, B. M. 2006, *ApJ*, 641, 689, doi: [10.1086/500572](https://doi.org/10.1086/500572)
- Wang, T., Brinkmann, W., & Bergeron, J. 1996, *A&A*, 309, 81
- Wilhite, B. C., Brunner, R. J., Grier, C. J., Schneider, D. P., & vanden Berk, D. E. 2008, *MNRAS*, 383, 1232, doi: [10.1111/j.1365-2966.2007.12655.x](https://doi.org/10.1111/j.1365-2966.2007.12655.x)
- Wisotzki, L. 2000, *A&A*, 353, 861
- Yang, J., Fan, X., Wu, X.-B., et al. 2017, *AJ*, 153, 184, doi: [10.3847/1538-3881/aa6577](https://doi.org/10.3847/1538-3881/aa6577)
- Yang, Q., Wu, X.-B., Fan, X., et al. 2018, *The Astrophysical Journal*, 862, 109, doi: [10.3847/1538-4357/aaca3a](https://doi.org/10.3847/1538-4357/aaca3a)
- Yang, Q., Shen, Y., Chen, Y.-C., et al. 2019, arXiv e-prints. <https://arxiv.org/abs/1904.10912>
- Zhu, F.-F., Wang, J.-X., Cai, Z.-Y., et al. 2018, *The Astrophysical Journal*, 860, 29, doi: [10.3847/1538-4357/aac2d7](https://doi.org/10.3847/1538-4357/aac2d7)
- Zu, Y., Kochanek, C. S., Kozłowski, S., & Udalski, A. 2013, *ApJ*, 765, 106, doi: [10.1088/0004-637X/765/2/106](https://doi.org/10.1088/0004-637X/765/2/106)
- Zu, Y., Kochanek, C. S., & Peterson, B. M. 2011, *ApJ*, 735, 80
- Zuo, W., Wu, X.-B., Liu, Y.-Q., & Jiao, C.-L. 2012, *The Astrophysical Journal*, 758, 104, doi: [10.1088/0004-637x/758/2/104](https://doi.org/10.1088/0004-637x/758/2/104)